J. Fluid Mech. (2005), *vol.* 526, *pp.* 19–66.
DOI: 10.1017/S0022112004002812 Printed in the United Kingdom

Highly resolved large-eddy simulation of separated flow in a channel with streamwise periodic constrictions

By JOCHEN FRÖHLICH[1], CHRISTOPHER. P. MELLEN[2], WOLFGANG RODI[2], LIONEL TEMMERMAN[3] AND MICHAEL A. LESCHZINER[3]

[1]Institute for Technical Chemistry and Polymer Chemistry, University of Karlsruhe, Kaiserstrasse 12, 76128 Karlsruhe, Germany

[2]Institute for Hydromechanics, University of Karlsruhe, Kaiserstrasse 12, 76128 Karlsruhe, Germany

[3]Imperial College of Science, Technology and Medicine, Department of Aeronautics, Prince Consort Rd, London SW7 2BY, UK

(Received 20 February 2004 and in revised form 29 September 2004)

High-resolution large-eddy simulation is used to investigate the mean and turbulence properties of a separated flow in a channel constricted by periodically distributed hill-shaped protrusions on one wall that obstruct the channel by 33% of its height and are arranged 9 hill heights apart. The geometry is a modification of an experimental configuration, the adaptation providing an extended region of post-reattachment recovery and allowing high-quality simulations to be performed at acceptable computing costs. The Reynolds number, based on the hill height and the bulk velocity above the crest is 10 595. The simulated domain is streamwise as well as spanwise periodic, extending from one hill crest to the next in the streamwise direction and over 4.5 hill heights in the spanwise direction. This arrangement minimizes uncertainties associated with boundary conditions and makes the flow an especially attractive generic test case for validating turbulence closures for statistically two-dimensional separation. The emphasis of the study is on elucidating the turbulence mechanisms associated with separation, recirculation reattachment, acceleration and wall proximity. Hence, careful attention has been paid to resolution, and a body-fitted, low-aspect-ratio, nearly orthogonal numerical grid of close to 5 million nodes has been used. Unusually, the results of two entirely independent simulations with different codes for identical flow and numerical conditions are compared and shown to agree closely. Results are included for mean velocity, Reynolds stresses, anisotropy measures, spectra and budgets for the Reynolds stresses. Moreover, an analysis of structural characteristics is undertaken on the basis of instantaneous realizations, and links to features observed in the statistical results are identified and interpreted. Among a number of interesting features, a distinct 'splatting' of eddies on the windward hill side following reattachment is observed, which generates strong spanwise fluctuations that are reflected, statistically, by the spanwise normal stress near the wall exceeding that of the streamwise stress by a substantial margin, despite the absence of spanwise strain.

1. Introduction

Flows that involve separation from curved surfaces occur in numerous engineering applications, in most of which the operational characteristics of the associated

components are materially sensitive to the details of the separation process. Examples are stalled wings and turbine blades, fuselages at high incidence, surface-vehicle bodies, streamlined obstacles, shaped constrictions or obstructions in pipes, highly curved ducts and jet-engine nacelles in cross-flow. Unfortunately, these flows are also among the most difficult to compute satisfactorily, whatever computational methodology is applied. Reynolds-averaged Navier–Stokes (RANS) schemes tend to perform especially badly, in that they predict widely disparate solutions with different turbulence models, even if these are variations of the same closure class, and they also generally display inconsistent performance across any significant range of separated flows (Manceau & Bonnet 2003; Jang *et al.* 2002; Wang, Yang & Leschziner 2004).

Among a number of challenging features of separation from continuous and curved surfaces is the strong spatial and temporal fluctuation of the separation line. The inevitable consequence of this process is that the time-averaged turbulent state of the flow around (or just upstream of) the time-averaged separation line does not scale with the wall distance in a manner consistent with the assumption of an attached boundary layer. This disparity has far-reaching implications for statistical closure strategies, because the state of the flow around the separation line impacts on the characteristics of the separated shear layer and on the reattachment process. Quite generally, the turbulent structures arising from separation are large, very vigorous and often accompanied by periodic components. This causes the whole recirculation region to be dominated by large-scale energetic eddies with strong deformation and dynamics, which are ill-described by one-point turbulence models that assume a high degree of 'locality' of turbulence. Another challenge, to any computational methodology, is the sensitive dependence of the mean reattachment location on that of separation. For the geometry considered in the present study, simulations with relatively coarse grids (Temmerman *et al.* 2003) as well as RANS studies (Manceau & Bonnet 2003) indicate that a 1% change in the predicted mean separation location goes hand-in-hand with a 7% change in the reattachment location, with obvious consequences for the gross flow properties, including pressure recovery. These characteristics imply that separation from curved surfaces demands, to a much greater extent than in flow separating from sharp edges, great care in the resolution and modelling of the near-wall flow, especially around the extensive separation region.

The available information on the fundamental physical processes playing a role in separation from curved surfaces is very limited. There are, in particular, very few results on turbulence characteristics and flow structure in the near-wall region within separation bubbles, the layer just upstream of separation and the immediate post-reattachment zone. While numerous experimental studies have been conducted on separated flow, their outcome has been mainly in the form of rather sparse data on statistical and global flow quantities, which do not provide much insight into the fundamental mechanisms of separation, reattachment and post-reattachment recovery. In addition, inevitable experimental limitations, associated with spanwise confinement, three-dimensional contamination and incomplete streamwise flow periodicity in configurations that are intentionally designed to be periodic (e.g. sinusoidally shaped surfaces), introduce significant uncertainties and errors.

Direct numerical simulations (DNS) offer, in principle, a route to information on separation processes, which experiments cannot provide. This is illustrated, for example, by the DNS of Alam & Sandham (2000) for suction-induced (laminar) separation from a flat plate and subsequent turbulent reattachment. However, at higher Reynolds numbers and in the presence of separation and geometric complexities, DNS is an extremely costly approach. This is due not merely to the very high resolution

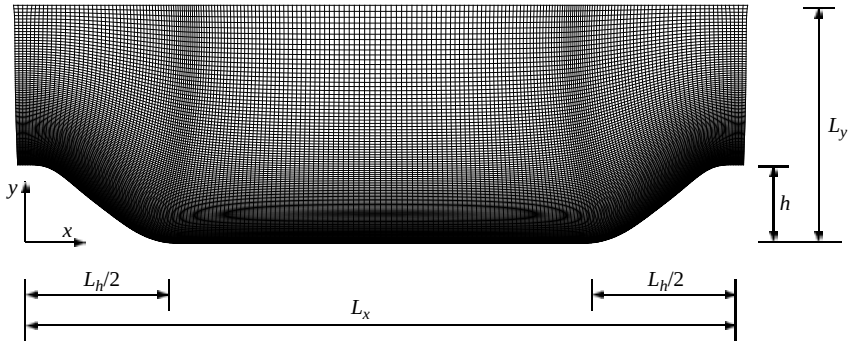

FIGURE 1. A two-dimensional slice of the geometry considered in the present paper together with the constitutive lengths and the coordinate system employed. The grid shown includes the two 'halo cells' on either side in the streamwise direction.

requirements, but also the extremely long integration times that are required to obtain reliable statistical information in the presence of large-scale and low-frequency structural features associated with the complex temporal and spatial variations in the separation and reattachment lines. At higher Reynolds numbers, equivalent to around 20 000 and above in a plane channel flow, the only economically tenable approach is to undertake highly resolved large-eddy simulations (LES) in carefully designed geometries for which any approximations adopted in relation to subgrid-scale processes and near-wall structure are demonstrably of no consequence to the accuracy of the quantities of interest. Such simulations not only offer insight into the physics of separation, but also provide valuable data for a wide range of statistical quantities against which turbulence closures as well as approximations adopted in the coarse-grid LES can be assessed. Both objectives are at the heart of the present paper. Indeed, some of the data contained herein have already been exploited to good effect in both RANS (Jang *et al.* 2002; Abe, Jang & Leschziner 2003) and LES studies (Temmerman *et al.* 2003). One set of data can be found in the ERCOFTAC database http://cfd.me.umist.ac.uk/ercoftac (case C81).

The geometry of the flow under consideration is shown in figure 1. It comprises a channel with periodically arranged hill-shaped constrictions on one wall (referred to as 'hills' henceforth). The simulation domain extends from one hill crest to the next. The spanwise direction is deliberately prescribed to be statistically homogeneous so as to secure statistical two-dimensionality. Streamwise periodicity and spanwise homogeneity thus free the simulations from uncertainties arising from boundary conditions, except for those at the upper and lower walls. The inter-hill distance is chosen so as to allow the flow to reattach well upstream of the following hill and permit some recovery before the acceleration on the windward side of that hill. The choice of this geometry is discussed in greater detail in § 2.

Simulations related to the present study have been performed on separated flows over wavy walls, e.g. by Armenio & Piomelli (2000), Henn & Sykes (1999) and Salvetti, Damiani & Beux (2001), in the context principally of atmospheric fluid mechanics. In all these studies, which are briefly reviewed in § 2, one objective has been to improve the understanding of the fundamental mechanisms associated with separation from curved surfaces. Additionally, the simulations were undertaken to derive information about the influence of geometric surface features (pitch, height) on the physical characteristics of the flow above them. Most LES computations for wavy-wall geometries are insufficiently resolved, however, or are for flows at very low

values of the Reynolds number. Also, the upper boundary is essentially open (i.e. the flow is practically unconfined), and the recirculation zone is either small or dictated by the relatively small hill-to-hill pitch. In contrast, the present geometry provides for a post-reattachment-recovery domain between successive hills, and the velocity field is highly resolved, especially in the recirculation zone, as detailed below.

The fact that streamwise periodicity and spanwise (statistical) homogeneity can be enforced virtually exactly, allows the type of geometry-induced contaminations, inevitably encountered in experimental studies, to be avoided. This is, self-evidently, an important advantage in using the simulation data for turbulence-model developments. On the other hand, some uncertainties arise from the imposition of instantaneous periodicity, and this calls for careful checks of decorrelation. A further important feature of the present investigation is that two quite independent simulations have been undertaken by two collaborating groups, using identical meshes, but different codes and subgrid-scale models. The high level of agreement of the two simulations reported herein thus strengthens confidence in their validity.

The remainder of the paper is organized in six sections. In § 2, the choice of geometry and flow conditions are discussed and justified by reference to previous studies, present objectives and computational constraints. The computational framework and the numerical parameters pertaining to the simulations reported later are described in § 3. Sections 4, 5 and 6 present and discuss different aspects of the results arising from the simulations. Statistical flow quantities are first covered in § 4. Section 5 then analyses the implications of instantaneous and unsteady flow features, with emphasis placed on structural aspects. Section 6 then returns to the statistical description dealing with spectra, anisotropy maps and two-point correlations. Conclusions are, finally, presented in § 7.

2. Choice of geometry and previous LES/DNS

This section discusses the motivation and arguments for selecting the present geometry, first introduced by Mellen, Fröhlich & Rodi (2000) and shown in figure 1. Throughout this paper, x, y and z identify, respectively, the streamwise, cross-flow and spanwise Cartesian coordinates. The geometry is akin to one studied experimentally by Almeida, Durao & Heitor (1993), which has been used as a test-case for an ERCOFTAC/IAHR workshop (Rodi, Bonnin & Buchal 1995), where a number of related RANS calculations were presented. The latter geometry consists of periodic hills of height h and separation $L_x = 4.5h$ in a channel of height $L_y = 6.07h$. The Reynolds number, based on the hill height and the bulk velocity, was 60 000. Preliminary LES calculations of this case by the present authors have shown that sufficiently well-resolved simulations would be too costly to undertake, because of the large channel height and the high Reynolds number. Also, during this ERCOFTAC/IAHR workshop, it was discovered that the experimental flow did not achieve a fully periodic state. Finally, because the duct carrying the flow was almost square in cross section, there were significant sidewall effects and hence significant departures from the two-dimensional state. For these reasons, it was decided to generate a new (synthetic) test case, specially designed to meet the objectives described in the Introduction.

Several substantial modifications were introduced to the experimental periodic-hill configuration of Almeida *et al.* (1993) in order to make fine-grid LES feasible. First, the Reynolds number was reduced to allow a near-DNS resolution at the lower wall, giving insignificant sensitivity to subgrid-scale and wall modelling. This reduction is not a fundamentally important drawback, as the key features of massively separated

flows are only weakly dependent on the Reynolds number. The value eventually chosen was $Re_h = 10\,595$, based on hill height and bulk velocity above the hill crest. Second, while the hill shape of the experimental configuration, having a streamwise extent of $L_h = 3.86h$, was retained, the inter-hill distance was substantially increased to $L_x = 9h$, and the channel height was reduced to $L_y = 3.035h$, resulting in a Reynolds number $Re_{L_y} = 21\,560$, based on L_y and the bulk velocity in the unconstricted channel. The reduction in channel height reduces significantly the number of grid points necessary. The increase in inter-hill distance enhances the streamwise decorrelation, permitting reattachment to take place on the plane portion between consecutive hills and introducing a post-reattachment-recovery region prior to a re-acceleration over the next hill. Streamwise decorrelation is highly desirable in channel-flow simulations using periodic streamwise conditions; typically, the length-to-height ratio of the calculation domain is chosen to be $L_x/L_y = \pi$. In contrast to the 'wavy-terrain' configuration, reattachment is here not enforced by the proximity of consecutive hills, rendering the behaviour of the separation region much more sensitive to the quality of the simulation and the modelling details, and hence presenting a more challenging test case. In order to limit the computational costs to an affordable amount, the spanwise extent of the calculation domain was chosen as $L_z = 4.5h$, and periodic conditions were applied at the spanwise boundaries. The adequacy of this choice is discussed in some detail in § 3.3.4.

As noted in the introduction, previous simulations akin to the present ones have been directed towards wavy-terrain geometries. These are characterized either by low Reynolds numbers or low resolution at high Reynolds numbers, weakly undulating hills provoking weak separation, or low pitch-to-hill-height values, all of which are counter to the present objectives. Most of these configurations feature a sinusoidally shaped lower wall with pitch λ. The simulations focus on the influence of the wavy wall on the boundary layer above the wave crests, with no significant relaxation of the disturbed flow between the waves being allowed. DNS computations have been performed in Maaß & Schumann (1996), De Angelis, Lombardi & Banerjee (1997) and Cherukat *et al.* (1998), for $h/\lambda = 0.1$. The conditions in these simulations correspond to the experiments of Hudson, Dykhno & Hanratty (1997) with the channel height being equal to λ and the Reynolds number based on hill height being only $Re_h = 676$. LES computations at Reynolds numbers not much higher are reported by Calhoun & Street (2001), Henn & Sykes (1999) and Armenio & Piomelli (2000). The statistical data obtained from such simulations match the experiment fairly well, as shown by the compilation of results given by Armenio & Piomelli (2000), but the Reynolds number in all of these calculations was simply too low for engineering interest, and re-attachment always occurred on the windward slope of the hills, so that there was no distinct post-reattachment-recovery region.

At higher Reynolds numbers, DNS is no longer possible, so that only LES can be carried out. LES of flow over a sinusoidal wall at $Re_\lambda = 4.2 \times 10^5$ were conducted by Salvetti *et al.* (2001). Although a very coarse grid was employed in combination with the no-slip condition, which is a questionable practice, the computed mean-velocity field was found to agree quite well with the experiments of Gong, Taylor & Dörnbrack (1996), but no results for turbulence quantities are presented. The influence of wave slope and Reynolds number was investigated by parameter variations, but a detailed analysis of the flow in the recirculation region or in the vicinity of the wall is not given. Henn & Sykes (1999) and Armenio & Piomelli (2000) reported LES results for the experimental situations studied by Buckles, Hanratty & Adrian (1984), in which case $h/\lambda = 0.2$ and $Re_h \approx 4800$, the latter being less than one half of the value

in the present study. Satisfactory agreement of mean flow and turbulent fluctuations with the experimental data was obtained, although separation was predicted to occur somewhat too early, and the separation bubble was too long as a consequence. An interesting observation made in this flow was that the spanwise velocity fluctuations were unusually large, relative to the level observed in flat-plate flow. However, the grid was not really fine enough near the hill wall, particularly in the spanwise direction, for this simulation to be regarded reliable.

The above discussion justifies the decision to undertake the present study on a new geometry. The chosen configuration combines carefully chosen geometric features and a reasonably high Reynolds number that together enable separation, recirculation and reattachment-related processes to be studied in much greater detail than has been done in earlier studies.

3. Computational framework

3.1. *Equations and numerical solution*

The Navier–Stokes equations for the resolved velocity $\overline{u_i}$ and the filtered pressure $\overline{p}$ are

$$\frac{\partial \overline{u}_i}{\partial x_i} = 0, \tag{3.1}$$

$$\frac{\partial \overline{u}_i}{\partial t} + \frac{\partial \overline{u}_i \overline{u}_j}{\partial x_j} = -\frac{\partial \overline{p}}{\partial x_i} + \frac{\partial (2\nu\, \overline{S}_{ij})}{\partial x_j} - \frac{\partial \tau_{ij}}{\partial x_j} + f, \tag{3.2}$$

with the filtered strain-rate tensor $\overline{S}_{ij} = \frac{1}{2}(\partial \overline{u}_i/\partial x_j + \partial \overline{u}_j/\partial x_i)$ and the molecular viscosity ν. The term $\tau_{ij} = \overline{u_i u_j} - \overline{u}_i \overline{u}_j$ results from the unresolved subgrid-scale contributions and needs to be modelled by an appropriate subgrid-scale (SGS) model. According to common practice, commutator terms are not explicitly accounted for.

The flow in the present streamwise periodic configuration is driven by a pressure gradient, here represented through the volume force f which is constant in space. Its magnitude is controlled so as to yield the desired global mass flux (at any instant). With this practice, the bulk flow is imposed exactly and is not a result of the simulation, as is the case, for example, in Salvetti *et al.* (2001), where the forcing term was fixed by an *a-priori* approximation of the drag.

Two entirely independent codes have been used to generate the present results. Both solve the equations for incompressible flow (3.1), (3.2) on body-fitted, curvilinear grids by a cell-centred finite-volume method with collocated storage for the Cartesian velocity components. Second-order central differencing is used for convection as well as diffusive terms.

The code LESOCC, employed by the University of Karlsruhe team (IfH), was originally developed by Breuer & Rodi (1994) with further enhanced in subsequent work (Mathey, Fröhlich & Rodi 1999; Mellen *et al.* 2000). A fractional step method is used, with a Runge–Kutta predictor and the solution of a pressure–correction equation in the final step acting as a corrector (Le & Moin 1991). The momentum interpolation proposed by Rhie & Chow (1983) is applied to inhibit spurious modes associated with the pressure–velocity coupling. The Poisson equation for the pressure increment is solved iteratively by means of the strongly implicit procedure (Stone 1968). Parallelization is implemented by domain decomposition, and explicit message passing is used, aided by two layers of halo cells along inter-domain boundaries for intermediate storage.

The Imperial College team (IC) used the code STREAMLES developed by Lardat & Leschziner (1998). The time scheme is based on an Adams–Bashforth predictor step and the solution of the Poisson equation for the pressure as corrector. Parallelization is effected by multi-block domain decomposition. Within this framework, the three-dimensional problem for the pressure is converted into a set of two-dimensional sub-problems by means of a Fourier transform in the periodic spanwise direction. Data are redistributed and the two-dimensional problems are then solved on individual processors by a SLOR technique applied in alternating directions together with V-cycle multigrid acceleration. Parallel efficiencies of 90% on partitions of up to 256 processors are obtained (Temmerman *et al.* 2000).

3.2. *Subgrid-scale modelling*

Two models of the eddy-viscosity type are employed in the computations presented below. Both model the anisotropic part of the SGS term as

$$\tau_{ij} - \tfrac{1}{3}\delta_{ij}\tau_{kk} = -2\nu_t \overline{S}_{ij} \tag{3.3}$$

(the trace τ_{kk} is lumped into a modified pressure), but differ in the way the eddy viscosity ν_t is determined.

In the LESOCC code, the dynamic Smagorinsky model (DSM) of Germano *et al.* (1991), with the modification of Lilly (1992), has been applied. The model coefficient C in the Smagorinsky expression

$$\nu_t = C\Delta^2|\overline{S}|, \qquad |\overline{S}| = (2\overline{S}_{ij}\overline{S}_{ij})^{1/2}, \tag{3.4}$$

with $\Delta = (\Delta x \Delta y \Delta z)^{1/3}$, is determined using an explicit box filter of width twice the mesh size in wall-parallel planes, together with averaging in the spanwise direction and relaxation in time with a factor of 10^{-3}. The near-wall behaviour of the DSM model in wall-resolving LES is such that it yields an eddy viscosity which is reduced naturally by the dynamic procedure as the wall is approached. Hence no explicit damping is required.

The second model is the 'wall-adapted local eddy-viscosity' (WALE) model proposed by Ducros, Nicoud & Poinsot (1998), which has been used in the computation performed with STREAMLES. In contrast to the Smagorinsky model which relates the viscosity to the symmetric part of the velocity-gradient tensor, $g_{ij} = \partial u_i/\partial x_j$, the WALE model is based on the symmetric part of the square of this tensor, $\overline{G}_{ij} = \frac{1}{2}(\overline{g}_{ik}\overline{g}_{kj} + \overline{g}_{jk}\overline{g}_{ki})$. Its traceless part, $\overline{G}^a_{ij} = \overline{G}_{ij} - \frac{1}{3}\delta_{ij}\overline{G}_{kk}$, is used to determine the eddy viscosity through

$$\nu_t = C_w\Delta^2 \frac{\left(\sqrt{|\overline{G}^a|}\right)^6}{|\overline{S}|^5 + \left(\sqrt{|\overline{G}^a|}\right)^5}. \tag{3.5}$$

It is demonstrated in Nicoud & Ducros (1999) that $|\overline{G}^a| = 0$ and hence $\nu_t = 0$ for the case of pure shear, e.g. $g_{ij} = 0$, except $g_{12} \neq 0$. This is effective near the wall, yielding the desired decay $\nu_t \sim y^{+3}$ (Ducros *et al.* 1998), and also in separated shear layers remote from walls, as illustrated by the results below. In contrast to the DSM, the reduction of ν_t with the WALE model only depends on the symmetry properties of the resolved motion, not on its smoothness. For the computation presented below, a value of $C_w = 0.1$ has been used (Ducros *et al.* 1998).

The distributions of the eddy viscosity ν_t obtained with the two independent calculations with the two SGS models at $x/h = 0.5$ and $x/h = 6.0$ are plotted in figure 2. The DSM yields a pronounced response in the shear layer emanating from the hill crest,

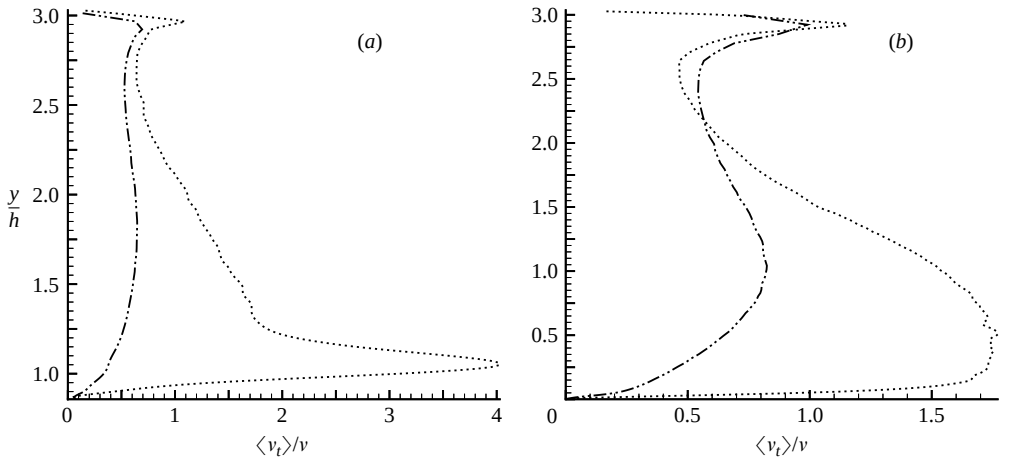

FIGURE 2. Subgrid-scale viscosity obtained in computations RUN 1 (dotted) and RUN 2 (dash-dotted) with the DSM and the WALE model, respectively. (*a*) $x/h = 0.5$, (*b*) $x/h = 6.0$.

giving fairly high ν_t values in the entire lower part of the flow. In contrast, the WALE model is not receptive to shear, as mentioned in connection with equation (3.5), so that it yields a lower eddy viscosity in most parts of the domain. The maximum value for ν_t/ν is approximately 5 with the DSM model, but only about 1 with the WALE model. While the difference is considerable, the influence of this difference on the LES calculations is low for the fine grid used here, as verified by the mean-velocity and turbulent-fluctuation profiles presented later. This confirms that the simulations are not materially inferior to a DNS near the lower wall. The influence of the SGS model is, of course, larger on coarser grids, and this has been studied in a companion paper (Temmerman *et al.* 2003) by performing calculations for the same test case on two coarser grids in combination with near-wall approximations. On the coarsest grid, some sensitivity to the SGS model was observed. On the medium grid, the influence was small, which gives further support to the claim of near-DNS quality of the present simulations for which the grids were substantially finer.

3.3. *Computational domain, grid and numerical parameters*

3.3.1. *Computational grid*

The computational domain ranges from crest to crest of two consecutive hills, separated by a distance of $L_x = 9h$. On the upper and lower side it is bounded, respectively, by a plane wall and the curved channel wall, respectively. The spanwise extent of the domain is $L_z = 4.5h$. The adequacy of these choices will be demonstrated later in this section.

For both computations reported below, exactly the same grid was employed one spanwise plane of which is shown in figure 1. Near the lower wall, where no-slip conditions are applied, a near-DNS representation is desired, so that reliable results, independent of any model assumptions, can be obtained in this region of primary interest. Hence, a fine enough grid must be used, which allows almost all motions, down to the dissipative scale, to be resolved. Also, numerical errors should be very small, so a high-quality nearly orthogonal grid is necessary. At the upper plane wall, the wall function of Werner & Wengle (1993) was used, since the details of the attached near-wall flow along this wall are not of interest here and do not affect the solution in the lower part.

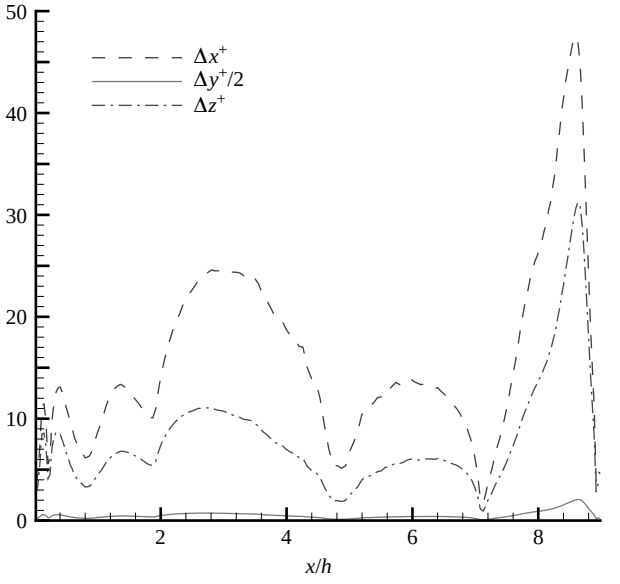

FIGURE 3. Extent of the wall-adjacent cells along the bottom boundary in wall units.

In view of the above desiderata, the structured, body-fitted curvilinear grid was carefully designed, with an elliptic grid-generation technique based on the approach of Steger & Sorenson (1979), as implemented by Mellen (1998). This yielded a high-quality mesh in the (x, y)-plane with almost orthogonal grid lines, an expansion ratio below 1.05 in the whole domain and a minimal streamwise gradation. This grid, shown in figure 1, contains $N_x \times N_y \times N_z = 196 \times 128 \times 186$ interior cells, with the spanwise distribution being uniform.† The quality of the resolution is judged first by determining the cell size in wall units, and figure 3 gives the size of the wall-adjacent cells in the three directions along the bottom wall. As seen, the centre of the wall-adjacent cell is located at $y_1^+ = \Delta y^+/2 \approx 0.5$ over most of the wall. The streamwise and spanwise cell sizes in wall units are below 25 and 10, respectively. These values are substantially lower than the recommendations $y_1^+ < 2$, $\Delta x^+ = 50$–150, $\Delta z^+ = 15$–40 given by Piomelli & Chasnov (1996) for wall-resolving LES. Figure 2 also shows that the normalized mesh distances increase along the windward slope of the hill due to an increase in the wall shear stress. The maximum values reached are $y_1^+ = 2$, $\Delta x^+ = 50$, $\Delta z^+ = 30$, all three still being within the recommended range given above.

Near the upper wall, the grid is considerably coarser and a wall function is used. The cell sizes along that wall are $\Delta x^+ = 12$–35, $\Delta z^+ = 10$–15 and $y_1^+ = 12$–17 in wall units, respectively. These values are within ranges in which wall functions are known to work well (Fröhlich & Rodi 2000), so that it can be expected that the effect of the upper wall on the flow in the lower part is adequately represented.

3.3.2. *Reference quantities and numerical parameters*

Throughout the paper, reference quantities for length, velocity and time are h, U_b and h/U_b, respectively, where U_b is the bulk velocity over the crest of the hill. All data presented are made dimensionless with these quantities. An overview of the

† The numbers given in Mellen *et al.* (2000) are slightly larger because halo cells required for periodic boundary conditions were counted while these are omitted herein.

Run	Grid	SGS	Wall	Code	$\Delta t/t_b$	t_{aver}/t_x	$\left(\frac{x}{h}\right)_{sep}$	$\left(\frac{x}{h}\right)_{reat}$
1	$196 \times 128 \times 186$	DSM	NS	LESOCC	2.7×10^{-3}	55	0.20	4.56
2	$196 \times 128 \times 186$	WALE	NS	STREAMLES	1.3×10^{-3}	55	0.22	4.72

TABLE 1. Parameters of the computations discussed in the present paper together with separation and reattachment points.

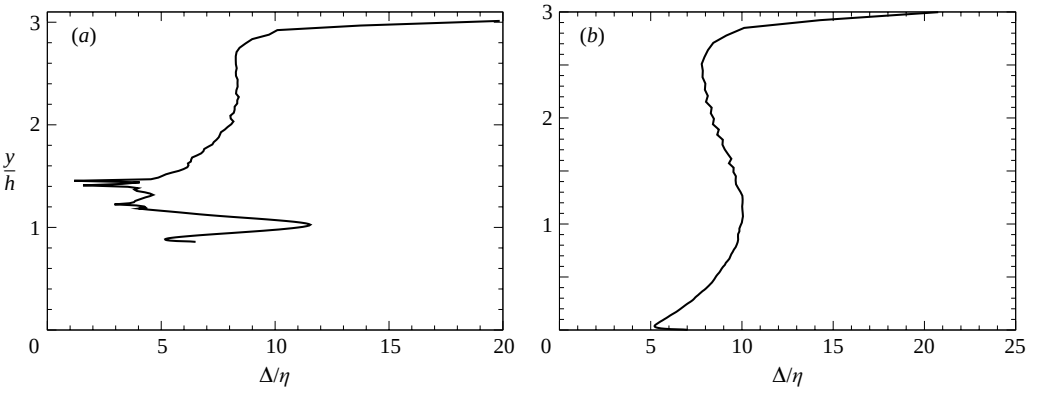

FIGURE 4. Profiles of the ratio Δ/η: (*a*) $x/h = 0.5$, (*b*) $x/h = 6$. Data from RUN 2.

numerical parameters used in the two independent calculations is given in table 1. The time step was chosen so as to result in a maximum local CFL number of 0.4 and 0.2, respectively. After 23 flow-through times, $t_x = L_x/U_b$, mean quantities were collected over a time period of $55t_x$ and were also averaged in the spanwise direction. The suitability of this integration period was checked by investigating changes in the statistics at intermediate times. Average quantities are denoted with angular brackets, and fluctuations with respect to the mean by a prime. In the remainder of the paper, the overbar designating resolved quantities is omitted for simplicity.

3.3.3. *Assessment of resolution*

The resolution characteristics of the grid near the walls have been discussed above by reference to the grid spacings in wall units. In the interior of the flow, the resolution can be assessed by comparing the grid spacing Δ to an estimate of the Kolmogorov length η, characterizing the length scale of the dissipative motion. The latter scale can be obtained from the dissipation rate ε by the relation

$$\eta = \left(\frac{\nu^3}{\varepsilon}\right)^{1/4}. \tag{3.6}$$

The dissipation rate was determined from the turbulence-energy budget, which will be presented and discussed in § 4 below. Figure 4 shows typical vertical profiles of the ratio Δ/η along cuts through the shear layer and in the region beyond reattachment. As seen, the ratio is of order 5 to 10. It should be noted that the numerical value of η resulting from (3.6) is a very conservative estimate for the finest scales in turbulent flow (Pope 2000). Equation (3.6) is merely a scale relation and should, in fact, contain a constant of value not neccessarily 1. Considering isotropic turbulence and a carefully devised model spectrum, Pope (2000) shows that the maximum dissipation takes place

at a wavenumber of $0.26/\eta$ corresponding to a length scale of about 24η. Since at least two grid points are needed to resolve a flow feature, a grid spacing of 12η is required to resolve features having a scale of 24η. With such a grid a substantial part of the dissipation is resolved. Figure 4 shows that this level of discretization has been achieved with levels $\Delta/\eta < 12$ over almost the entire domain, except near the upper wall where resolution is not of major concern, as noted earlier.

Further support is provided by the ratio ν_t/ν which gives an indication of the ratio of resolved and modelled contributions to dissipation. Figure 2 suggests that, typically, half of the dissipation results from the SGS model when the WALE model is used, while the remainder is associated with the resolved motion. This indicates a very good resolution for this relatively high-Reynolds-number flow. When the dynamic model is used, the eddy viscosity is larger and so is the modelled contribution. Nevertheless, the results for the mean flow and the turbulence fields reported below agree to a remarkable degree which gives evidence of the low contribution of the SGS model to the first and second moments.

The quality of resolution can further be assessed by means of spectra. One of the most critical areas in terms of resolution is the thin attached boundary layer separating from the hill and entering a region where the grid gradually coarsens (see figure 1). Spectra have been computed in this region and are reported in § 5.1 below. As will emerge, these also indicate a good resolution with the grid and method employed.

It should be stressed here that, with LES quantities related to low wavenumbers can be well resolved, while others related to high wavenumbers, such as dissipation, are not. Hence, the assessment of resolution in an LES must be related to the quantity under consideration. The quantities extracted from the present simulations and discussed below relate to low-order moments of the velocity which are largely due to low-wavenumber contributions in turbulent flows. For high Reynolds numbers these can be computed accurately by LES, in terms of their statistical properties, even if the dissipation range is not resolved at all. In the present medium-Reynolds-number case this is similarly achieved by also resolving a significant part of the dissipation range.

3.3.4. *Extent of the calculation domain*

It has been observed in spanwise-homogeneous, statistically two-dimensional separated flows that structures with especially large scales in the spanwise direction may exist, as is the case in the flow around a cylinder (Zdravkovich 1997). If computations are performed on a domain the spanwise extent of which is smaller than these scales, these structures cannot be represented adequately so that an error is introduced. In the following we investigate whether the spanwise extent of $4.5h$, chosen to keep the computational cost affordable for the high-resolution LES, is sufficient. To this end, a sensitivity study was performed in which the spanwise domain size was increased, with all other parameters being unchanged. However, this had to be done on a substantially coarser grid for cost reasons. This contains $N_x \times N_y = 112 \times 64$ points in the (x, y)-plane and requires the use of a wall function on the lower curved wall also. Here, the wall function of Werner & Wengle (1993) was used, together with the DSM subgrid-scale model in two calculations, one performed with a spanwise extent of $L_z/h = 4.5$ and $N_z = 90$ points in the spanwise direction, and the other with $L_z/h = 9$ and $N_z = 188$ points (Mellen *et al.* 2000). Typical results of this study are given in figure 5, which shows profiles of the streamwise mean velocity and fluctuations at $x/h = 2.0$. The average separation point changes from $x_{sep}/h = 0.50$ to 0.45 and the reattachment point from $x_{reat}/h = 3.20$ to 3.25 when halving the size of the spanwise domain. There is hardly any change in the mean-velocity profiles, but there are

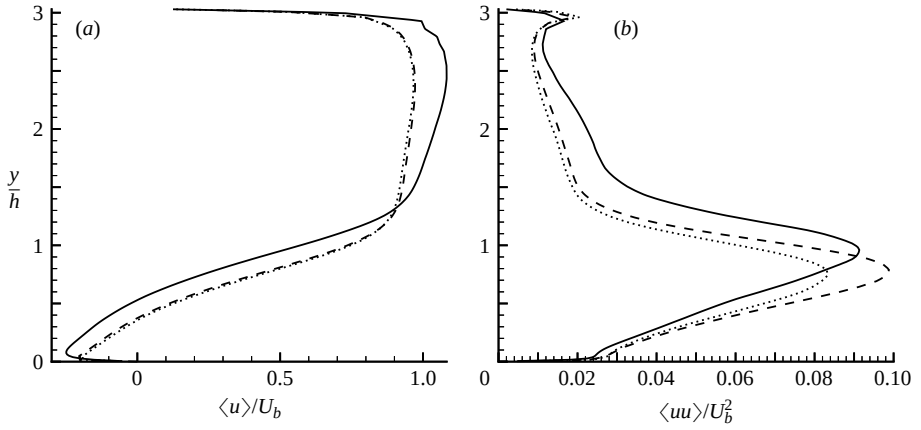

FIGURE 5. Computations with different lateral domain sizes, $L_z/h = 4.5$ (dotted) and $L_z/h = 9$ (dashed) on coarser grids. (*a*) Average velocity at $x/h = 2.0$, (*b*) streamwise fluctuations at $x/h = 2.0$. The data from the corresponding fine-grid computation RUN 1 with $L_z/h = 4.5$ (solid) have been added for comparison.

changes in the peak level of the u-fluctuations. The inclusion of the highly-resolved results in figure 5 indicates, however, that the sensitivity to the spanwise extent is substantially lower than that to the resolution and near-wall treatment. Thus, the effect of the spanwise extent increasing beyond $4.5h$ is judged to be minor.

Another, more fundamental test of the adequacy of the chosen spanwise extent is to compute two-point correlations, which give an indication of the spanwise extent of the structures. The size of the structures is roughly twice the distance between the origin and the point where the correlation levels off to zero. Hence, the calculation domain is usually considered large enough if all two-point correlations vanish at half the domain width. The definition of the correlation coefficient used here is

$$R_{\phi\psi} = \frac{\langle \phi\psi \rangle}{\sqrt{\langle \phi\phi \rangle \langle \psi\psi \rangle}} \tag{3.7}$$

where ϕ and ψ are two fluctuating quantities. In the following, we consider the correlation coefficient of the u-, v- and w-fluctuations, denoted R_{11}, R_{22}, R_{33}, respectively, as a function of the separation d_z in the z-direction. This was done for several points in the (x, y)-plane for the simulation of the domain with $L_z/h = 9$. The averaging was performed in time and over several pairs of points with the same (x, y)-coordinates and distance r_z, but each at a different position in z. The distributions of R_{uu} are shown in figure 6 for the locations identified in the inset. It is apparent that immediately after separation (point A), the correlation length, and hence the size of the spanwise structures, the correlation effectively vanishes at $1.5h$. Further downstream, at points C and E, a pronounced minimum develops, which is due to the formation of streamwise vortices discussed later. This is reduced within the recirculation region and even more so when the leeward side of the hill is approached (not shown here). Close to the upper boundary (point B), no pronounced minimum is observed. From figure 6 it is clear that the correlation does not vanish for all points in the domain within $r_z = 2.25h$ (half the domain size), so that the largest scales cannot be fully represented in the computation. A spanwise extent of $L_z/h \approx 7$–8 would possibly be required to achieve this. A computation with this domain size, while maintaining the spatial resolution, was not possible with the computer resources available. Figures 5 and 6

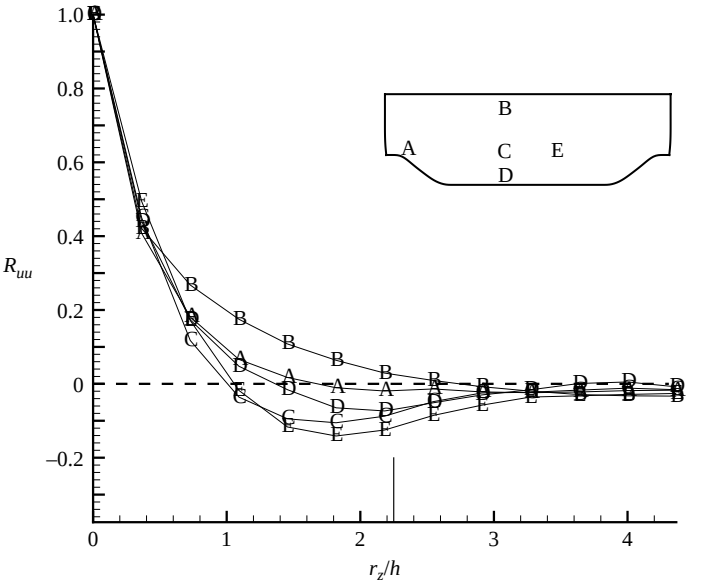

FIGURE 6. Spanwise correlation of streamwise velocity obtained with $L_z = 9h$, at different points $(x/h, y/h)$ in the flow field. A: (0.4, 1.1), B: (3.6, 2.5), C: (3.6, 1.1), D: (3.6, 0.2), E: (5.4, 1.1). The short vertical line relates to the size of the domain with $L_z = 4.5h$. Data from Klostermeier (2001).

suggest, however, that the error introduced in the first- and second-order moments is small. As reported in many bifurcation studies, e.g. the dissertation of Fröhlich (1990), reducing the domain width from the optimal size tends to 'squeeze' only the very largest structures. In the presence of a wide range of lengths this does not substantially alter the primary flow properties.

It is finally remarked that, if used as a test case, the issue of fully adequate (optimal) spanwise extent only affects comparisons with solutions based on the assumption of complete spanwise homogeneity, as is the case with two-dimensional RANS computations. If, in contrast, LES or DNS computations are undertaken with the same spanwise periodicity imposed, the comparison of the associated results is not affected.

Consideration is next given to the extent of the computational domain in the streamwise direction. For 'wavy-terrain' simulations the computational domain usually extends over two periods of the sinusoidal wall, and it was demonstrated by Calhoun (1998) and Henn & Sykes (1999) that this is indeed sufficient. Since the present geomety features a substantially larger inter-hill distance and a reduced channel height, one period was selected as the computational domain. The analysis of the instantaneous flow in § 6 and the spectra in § 5.1 below demonstrates that the low-frequency contributions to the temporal spectra result mainly from the return time of the periodic flow and not from the size of the structures in the streamwise direction. RANS computations contributed to a recent ERCOFTAC/IAHR workshop (Manceau & Bonnet 2003) also point to this conclusion. These were performed over two periodic segments with inflow conditions taken from the LES, and showed only insignificant differences between the consecutive segments. Further validation was provided by Temmerman (2004) who performed simulations over two streamwise segments on a grid of $112 \times 64 \times 56$ cells per segment and $L_z = 4.5h$. Differences in mean flow and the

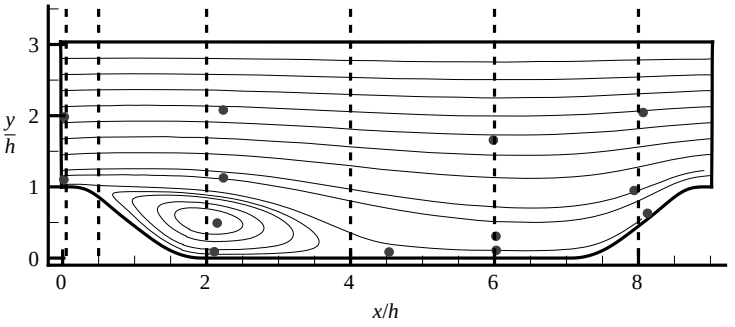

FIGURE 7. Streamlines of the average flow and location of cuts at $x/h = 0.05, 0.5, 2, 4, 6, 8$ where detailed data analysis has been performed. The dots indicate the locations where spectra have been computed.

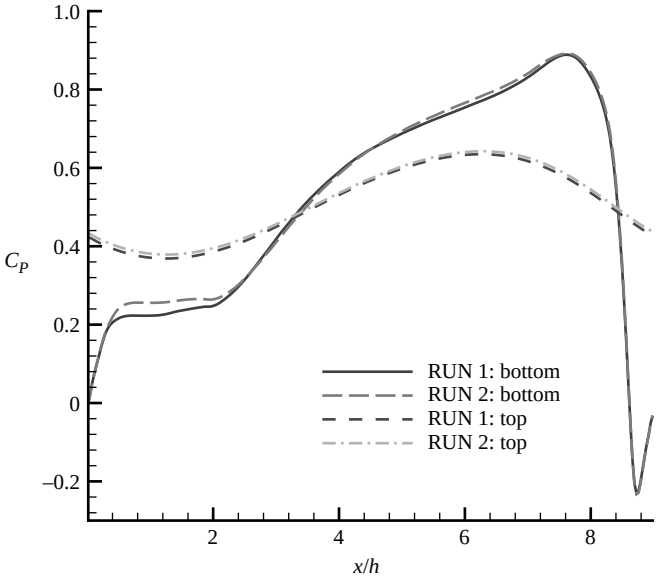

FIGURE 8. Pressure coefficient along the top and bottom wall from RUN 1 and RUN 2 with normalization as discussed in the text.

fluctuations, compared to the single-segment computation were extremly small. It is concluded, therefore, that one streamwise segment is sufficient for the present study.

4. Results for statistically averaged quantities

4.1. *General view of the flow*

Before profiles of various statistically averaged quantities are presented at a number of streamwise stations, some major global flow characteristics are shown in figures 7 to 9. Figure 7 shows the time-averaged streamlines, together with the locations at which statistical data are presented in subsections to follow.

The flow separates at $0.2h$ downstream of the hill crest and reattaches at $4.6h$–$4.7h$. Thus, the recirculation zone occupies about 50% of the streamwise domain. The flow then recovers for about $2.5h$, after which it accelerates towards the next hill

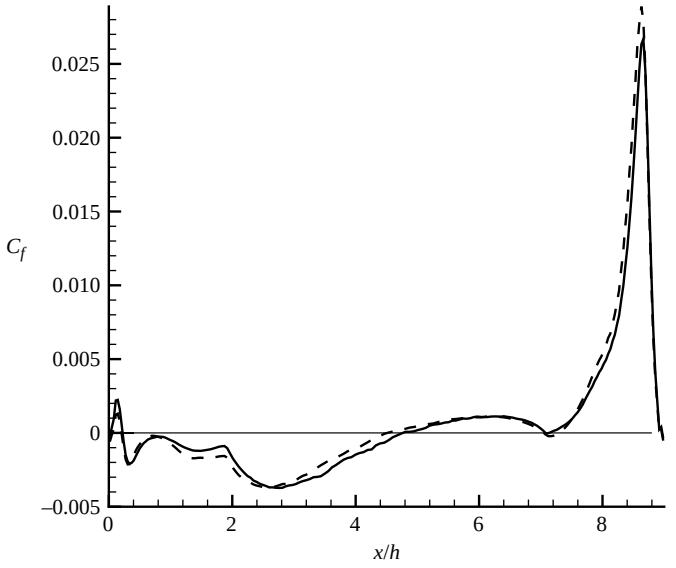

FIGURE 9. Comparison of friction coefficient along bottom wall: RUN 1 (dashed), RUN 2 (solid).

crest. The skin-friction distribution on the lower wall, given in figure 9, indicates a rather irregular, geometry-induced variation of the near-wall velocity. This is best considered in conjunction with the wall-pressure coefficient on the lower and upper walls, given in figure 8. As the reverse flow in the recirculation region approaches the leeward hill face, it decelerates and almost reverses its direction, implying a trend towards the formation of two secondary vortices immediately following separation. The pressure coefficient on the lower wall is almost constant over most of the upstream half of the recirculation zone, following the sharp rise immediately downstream of the crest, which provokes separation. The pressure plateau in this area is typical of that generally observed in separated regions bordered by an outer flow with minor streamwise velocity variations, and is entirely consistent with the very slow near-wall flow in the region $0.5 < x/h < 2.0$. Following a minimum in skin friction at $x/h = 2.8$, where the reverse flow reaches a maximum, the near-wall velocity and skin friction increase towards zero at the reattachment point, and this is consistent with a positive pressure gradient associated with the deceleration of the outer flow as the lateral dimension of the recirculation zone diminishes and the outer flow decelerates. After reattachment and partial recovery, subject to a moderately adverse pressure gradient, the developing boundary layer is decelerated by the steep windward face of the next hill, to the extent of becoming incipiently separated at $x/h = 7.2$. The local minimum in skin friction at this location coincides with an increase in wall-pressure gradient at the same location, which is at the foot of the right-hand hill. The flow finally accelerates on the windward hill side towards the hill crest. As it does so, the friction coefficient rises sharply, and the thickness of the boundary layer decreases from $d \approx 0.2h$ at the foot of the hill to $d \approx 0.08h$ just upstream of the hill crest. The strong increase in shear stress in this region is responsible for the higher y_1^+ values observed in figure 3.

The two simulations are seen to yield distributions which agree closely, with RUN 1 giving a slightly shorter reattachment length and marginal separation at the foot of

the downstream hill. Associated with the slightly shorter recirculation length is a slightly higher rate of pressure around $3 < x/h < 5$, and this is also the reason for the lower pressure level in the upstream half of the recirculation zone.

4.2. *Profiles of statistical properties*

In what follows, profiles of mean velocity components, turbulent stresses, turbulence energy and budgets for the stresses and energy at the streamwise stations indicated in figure 7 are presented and discussed in figures 10–14. The stations were chosen so as to represent flow regions having particular characteristics or behavioural features. The profiles of velocity and stresses are presented over the full height of the channel from the lower to the upper wall, while the budgets are only given for the lower portion of the flow, extending to $y/h = 2$, a layer in which all the physical processes of prime interest occur. Profiles of mean velocity, turbulent stresses and turbulence energy are included from both runs and are thus juxtaposed. The profiles are plotted as pairs arising from the two simulations. Because the profiles forming any one pair generally agree closely, they can be readily recognized as being associated. Attention is drawn to the fact that the turbulence energy is plotted as $-k/U_b^2$, i.e. these profiles thus appear to the left of the zero origin of the abscissa.

The budgets arise from the various terms contributing to the transport equation for the Reynolds stresses $\langle u_i' u_j' \rangle$,

$$\frac{\mathrm{D}}{\mathrm{D}t}\langle u_i' u_j' \rangle = P_{ij} + T_{ij} + D_{ij} + D_{p,ij} + \Phi_{ij} - \varepsilon_{ij} \tag{4.1}$$

with the right-hand-side terms defined as follows:

$$\text{production} \qquad P_{ij} = -\langle u_j' u_k' \rangle \frac{\partial \langle u_i \rangle}{\partial x_k} - \langle u_i' u_k' \rangle \frac{\partial \langle u_j \rangle}{\partial x_k}, \tag{4.2}$$

$$\text{turbulent transport} \qquad T_{ij} = -\frac{\partial \langle u_i' u_j' u_k' \rangle}{\partial x_k}, \tag{4.3}$$

$$\text{viscous diffusion} \qquad D_{ij} = \nu \frac{\partial^2 \langle u_i' u_j' \rangle}{\partial x_k \partial x_k}, \tag{4.4}$$

$$\text{pressure diffusion} \qquad D_{p,ij} = -\frac{1}{\rho}\left(\frac{\partial \langle u_j' p' \rangle}{\partial x_i} + \frac{\partial \langle u_i' p' \rangle}{\partial x_j} \right), \tag{4.5}$$

$$\text{pressure strain} \qquad \Phi_{ij} = \left\langle \frac{p'}{\rho}\left(\frac{\partial u_i'}{\partial x_j} + \frac{\partial u_j'}{\partial x_i} \right) \right\rangle, \tag{4.6}$$

$$\text{dissipation} \qquad \varepsilon_{ij} = 2\nu \left\langle \frac{\partial u_i'}{\partial x_k} \frac{\partial u_j'}{\partial x_k} \right\rangle. \tag{4.7}$$

The terms (4.2)–(4.6) were determined explicitly from the IC simulation (RUN 2), while ε_{ij} was obtained as the imbalance of the other terms according to (4.1). An explicit evaluation of ε_{ij} yielded approximately 50–70% of the value obtained from the balance, a level regarded as reasonable in view of the fact that the ratio of grid distance to Kolmogorov length was of order 10. This level is consistent with the ratio $\nu_t/\nu = O(0.5)$ in figure 2.

The budget for the turbulence energy $\langle k \rangle = \langle u_i' u_i' \rangle$ follows from contracting the set of stress equations, i.e. from half of the sum of the equations for $\langle u'u' \rangle$, $\langle v'v' \rangle$, and $\langle w'w' \rangle$. In this, the pressure–strain term should vanish, and this has been confirmed to be closely satisfied by summing the pressure–strain contributions to the normal-stress budgets. Attention is drawn to the fact that the symbols attached to the budget

profiles only serve to identify the different lines more clearly and do not correspond to the computational grid employed.

4.3. *Position* $x/h = 0.05$

This location is a short distance beyond the hill crest. Profiles of velocity, Reynolds stresses and turbulence energy at this position are given in figure 10(a, b). Budgets, although available, are not included here, however, because the extremely high gradients and rates of change of the flow variables very close to the wall pose uncertainties in relation to the accuracy of the higher-order moments contributing to the budgets.

The boundary layer is very thin (about $0.1h$), and the streamwise velocity features a near-wall peak, due to the preceding acceleration along the windward slope of the hill. There is also a slight upward motion associated with flow along the steeply inclined windward hill face. The shear stress $\langle u'v' \rangle$ reaches a first minimum value in the boundary layer and then declines to virtually zero, where the velocity component $\langle u \rangle$ has a maximum. However, beyond this location, the velocity gradient reverses sign, but the shear stress does not. Indeed, the maximum $\langle u'v' \rangle$ occurs where there is a local minimum of $\langle u \rangle$ at around $y/h = 1.6$, which is in conflict with the eddy-viscosity concept and indicates substantial stress-transport effects (unless $\partial \langle v \rangle / \partial x$ is important, which is not the case). The velocity then rises to a second maximum towards the upper wall, and the shear stress decreases, changing sign roughly at the location of this maximum and reaching a peak value in the boundary layer near the upper wall, both consistent with the eddy-viscosity concept.

The normal stresses are remarkable, primarily in so far as their respective maxima occur at very different positions, giving rise to very high local levels of anisotropy. The streamwise stress $\langle u'u' \rangle$ has a strong peak close to the lower wall, reflecting intense generation by the high shear strain in the boundary layer. As expected, the spanwise stress is lower and the wall-normal stress is the lowest. However, their maxima occur well outside the boundary layer, suggesting a dominant history effect from upstream locations. In the boundary layer, the anisotropy is unusually intense, with the ratio $\langle u'u' \rangle / \langle v'v' \rangle$ reaching a value of order 20 and indicating the approach to two-component turbulence necessarily prevailing close to the wall due to the wall's blocking effect. The very high near-wall level of $\langle u'u' \rangle$ is also due to intense streamwise fluctuations associated with intermittently high positive and negative velocities that arise because the separation moves quickly over a substantial proportion of the surface around the hill crest. As will become clear later, the high level of spanwise stress $\langle w'w' \rangle$ at around $y/h = 1.08$ is linked to an intense amplification of this component upstream of the hill crest by the action of 'splatting' on the windward slope and the subsequent transport of this component towards the crest region. Away from the lower wall, in the weak and zero-shear regions, the normal stresses, and thus the turbulence energy, are maintained at fairly high levels, again indicating intense transport of turbulence from the highly disturbed upstream region.

4.4. *Position* $x/h = 2.0$

This location is in the middle of the recirculation region and is therefore especially interesting, as it combines three interacting layers: the free shear layer separating from the hill crest, the reverse flow below this layer, i.e. for $y/h \leqslant 0.5$ consisting also of a free shear layer, and a boundary layer below $y/h = 0.1$. Profiles pertaining to this section are included in figures 10(c), 10(d), and 12, the last containing the budgets. The streamwise velocity profiles are unremarkable and show the expected reverse flow in the lower portion, the shear layer above it and the boundary layer at the upper

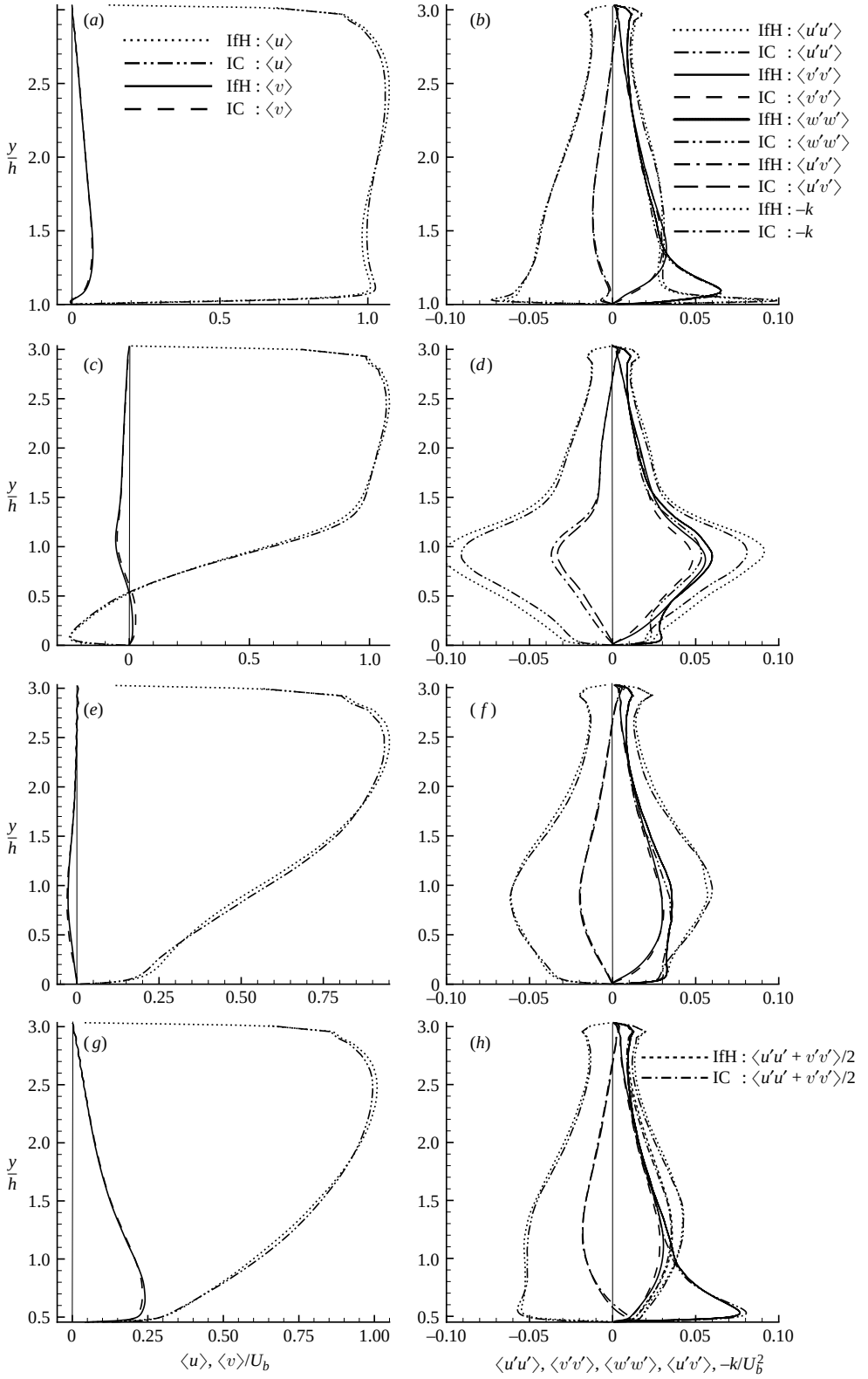

FIGURE 10. For caption see facing page.

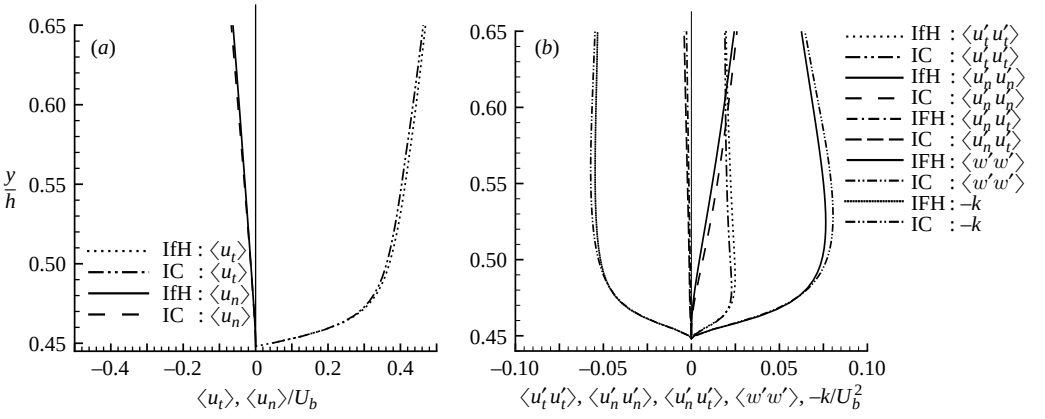

FIGURE 11. (*a*) Mean velocities and (*b*) Reynolds stresses in a zoom close to the wall at $x/h = 8$. In contrast to the graphs in figure 10, a decomposition of the velocity vector into wall-normal components (index n) and tangential components (index t) has been applied here.

wall, with the slight glitch in $\langle u \rangle$ originating from the application of the log-based wall law at this wall. The transverse velocity is insignificant, as this section is, effectively, in the streamwise centre of the recirculation bubble. The Reynolds stresses in the shear layer conform to expectations: the shear stress is negative, and all stresses reach a peak at the location of maximum shear strain. Of the normal stresses, the streamwise stress is the highest, while both the spanwise and transverse stresses are lower and of very similar shape and magnitude, indicating that, in the absence of significant wall influences, the pressure–strain process is unbiased in respect of these two stresses. The anisotropy is significant, but not intense, with the ratio $\langle u'u' \rangle / \langle v'v' \rangle$ of order 1.3. Also as expected, the ratio $\langle u'v' \rangle / k$ is about 0.3.

In the reverse-flow layer, $0 < y/h < 0.5$, the most interesting feature, found by both simulations, is the distinctive rise of $\langle w'w' \rangle$, relative to the other two normal stresses, leading to a virtual equality of the spanwise and streamwise normal stresses close to the wall. A similar behaviour will be shown later to occur at $x/h = 6$, and this is claimed to be due to 'splatting' effects around the reattachment region, which are then carried along to neighbouring locations by transport. This will be discussed further at the end of this subsection by reference to the budget at $x/h = 2$. Splatting will also be seen later to be an exceptionally influential process in the accelerating portion above the windward face of the right-hand hill. In contrast, the wall-normal stress declines steadily as the wall is approached, a behaviour anticipated due to wall blocking. A feature that is not expected, however, is that the reversal in the streamwise-velocity gradient close to the lower wall, at $y/h = 0.1$, is not accompanied by a corresponding

FIGURE 10. Comparison of mean velocities and Reynolds stresses obtained in the two independent computations RUN 1 (IFH) and RUN 2 (IC). The profiles have been determined at $x/h = 0.05$ (a, b), $x/h = 2$ (c, d), $x/h = 6$ (e, f), $x/h = 8$ (g, h). The left-hand pictures (a, c, e, g) show profiles of the mean velocities $\langle u \rangle$ and $\langle v \rangle$ according to the keys in graph (a). The pictures on the right hand side (b, d, f, h) display the Reynolds stresses, again according to the keys in the uppermost graph. Subfigure (h) contains two further lines with the additional keys indicated in this graph. Different quantities can be identified with more ease when considering a pair of lines for the same value. Observe that the vertical axis is different in some plots due to the elevation of the bottom surface.

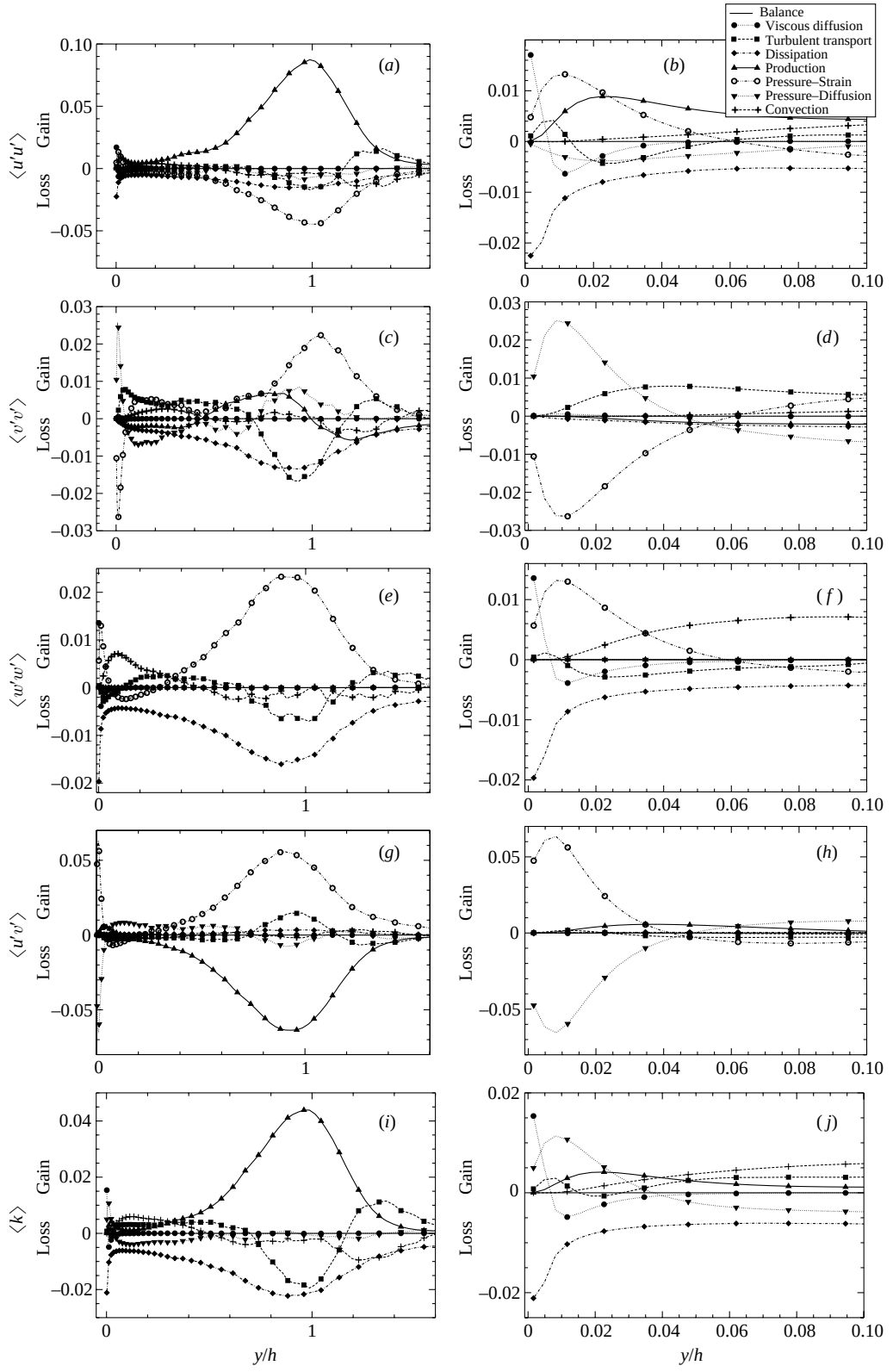

FIGURE 12. For caption see facing page.

reversal in the shear stress, anticipated on the basis of the eddy-viscosity concept. It follows that the turbulent shear stress cannot support the negative wall shear stress in this region, which must exist due to the reverse motion, as seen in figure 9 (note that correlation $\langle u'v' \rangle$ and the shear stress $\langle \tau \rangle$ have opposite signs). Hence, the viscous stress must dominate in this region.

As will be demonstrated later when examining the budgets, the processes in the near-wall layer under consideration differ drastically from those in a conventional boundary layer. For example, although there is a sign reversal in the production of the shear stress, in line with the sign reversal in the shear strain, other contributions to the shear-stress balance conspire to maintain the shear stress at a positive level. Moreover, the increase of the turbulence energy and the wall-parallel normal stresses, due to a combination of production, splatting-related phenomena and convective transport, leads to very high levels of near-wall anisotropy and ratio $\langle u'v' \rangle / k$, even outside the buffer layer, the position of which corresponds to $y/h = 0.05$, i.e. well below the location of minimum reverse velocity.

The budgets of all stresses and turbulence energy are given in figure 11. They cover only the lower region, roughly to the upper edge of the separated shear layer, as this region is of primary interest. The shear-stress budget shows the usual behaviour in the separated shear layer of a near balance between pressure–strain and production, with the remaining terms being subordinate. As the wall is approached, but outside the viscous sublayer ($y/h > 0.05$), the influence of production diminishes, and the pressure–strain becomes negative and is increasingly balanced by the positive pressure diffusion. As the position of peak negative velocity is traversed, the production reverses sign, but remains low relative to pressure diffusion, a condition that prevents the shear stress from changing sign, as noted earlier. As the viscous sublayer is entered, the production reaches a weak maximum, but this is insufficient to counter the rapidly declining shear stress, which therefore remains positive. Within the viscous sublayer, pressure–strain rises strongly together with a corresponding drop in pressure diffusion, with both essentially balancing each other. At the wall itself, neither is constrained to vanish, because one constituent of both involves the correlation of pressure fluctuation and wall-normal gradient of the streamwise-velocity fluctuation, neither of which asymptotes to zero at the wall.

The $\langle k \rangle$-budget shows that production is highest in the separated shear layer, thus causing a maximum in $\langle k \rangle$. At the position of peak production the ratio of production to dissipation is around 2. Turbulent diffusion accounts for most of this imbalance, transporting energy away from the production region to the reverse-flow region and to the edge of the shear layer. This explains the elevated values of $\langle k \rangle$ in the outer region despite the low velocity gradient and hence low production therein. Convection is also significant at the edges of the shear layer. At the outer edge, it removes energy to regions further downstream, while in the reverse-flow region, energy is gained through convective transport from the reattachment region. Above the boundary layer, production is low in the reverse-flow region, with positive convection and turbulence transport balanced by dissipation and pressure diffusion. Hence, the characteristics of this region are very different from those in a conventional mixing layer. As is the case

FIGURE 12. Budgets of Reynolds stresses and $\langle k \rangle$ at $x/h = 2$. Left: principal part of the channel, right: zoom onto the bottom wall. Symbols in these figures and similar ones below serve to distinguish lines and do not represent the inter-nodal distance of the computational grid employed.

with shear-stress production, that of turbulence energy also rises to a weak maximum very close to the wall, but its contribution to the balance is generally small. Within the viscous sublayer, pressure and viscous diffusion become the dominant gain terms, while dissipation becomes the dominant sink. As expected, the balance asymptotes to a condition in which viscous diffusion is cancelled by dissipation, with all other terms vanishing at the wall.

The budget for $\langle u'u' \rangle$ shares a number of features with the budget for $\langle k \rangle$. Thus, the productions show similar profiles, with that of $\langle u'u' \rangle$ having a level about twice that of $\langle k \rangle$, since the production of $\langle w'w' \rangle$ is zero, while that of $\langle v'v' \rangle$ is negligible. On the other hand, the dissipation levels of all three normal stresses in the shear layer are similar, consistent with the concept of isotropy in the smallest scales. The imbalance between production and dissipation is compensated mainly by the pressure–strain term, which extracts energy from the $\langle u'u' \rangle$ component and transfers this to the other normal stresses, the balance of which thus feature positive pressure–strain contributions. In the near-wall region, outside the viscous sublayer, the budget of $\langle w'w' \rangle$ is dominated by positive convection and negative dissipation and pressure–strain. The positive convection term reflects the transport of high levels of $\langle w'w' \rangle$ from the impingement zone in which splatting is an important mechanism. As shown earlier, the consequence is a sharp increase in $\langle w'w' \rangle$, which reaches a level very close to that of $\langle u'u' \rangle$. It is this process that causes a reversal in the pressure–strain contribution, with both $\langle u'u' \rangle$ and $\langle w'w' \rangle$ transferring energy to $\langle v'v' \rangle$. As the wall is approached, within the thin boundary layer, $\langle v'v' \rangle$ has to decay rapidly, and this is effected by a reversal in the pressure–strain, which now transfers energy from $\langle v'v' \rangle$ to $\langle u'u' \rangle$ and $\langle w'w' \rangle$. Positive convective transport remains an important contributor to $\langle w'w' \rangle$, keeping this stress relatively high in the boundary layer. As the viscous sublayer is traversed, viscous diffusion tends to balance dissipation, as is the case with $\langle k \rangle$. In the case of $\langle v'v' \rangle$, in contrast, viscous diffusion is necessarily negligible and dissipation approaches zero as turbulence (including the smallest scales) tends towards a two-component state. The balance is dominated by pressure–strain, which has to diminish $\langle v'v' \rangle$ at a rate proportional to y^4, and pressure diffusion.

4.5. *Position* $x/h = 6.0$

This location is within the post-reattachment region, halfway between reattachment and the foot of the next hill. The flow here consists of the boundary layer developing from the reattachment point and, above it, a wake which originates from the separated shear layer further upstream. It is thus characterized by flow components with very different scales and history which interact to form a flow recovering towards a fully developed channel flow. It is well known that most statistical closures do not represent this recovery process well. The features discussed in this section will therefore be of particular interest to modellers.

Profiles of velocity and second moments are shown in figure 10(*e*, *f*). The boundary layer, of thickness $y \approx 0.2h$ is bordered by a region of nearly constant velocity gradient, reflecting an ongoing recovery of the reattached shear layer. As seen from figure 8, the flow develops against an adverse pressure gradient, caused by the outer flow decelerating mildly as fluid is transported downwards to fill the wake. The boundary layer at the upper wall is much thicker, of order $y = 0.6h$, and its structure is expected to conform to that of other boundary layers subjected to a mild adverse pressure gradient.

Although the flow in this section is drastically different from that at $x = 2h$, the turbulence field is characterized by qualitatively similar features, except that the intensity

of turbulence is now much reduced as the strain diminishes and the flow tends to approach a state of equilibrium. Thus, the stresses and turbulence energy reach maxima within the high-strain region of the shear layer, the ratio $\langle u'v' \rangle / \langle k \rangle$ being close to 0.3, and the $\langle u'u' \rangle$ exceeding $\langle w'w' \rangle$ by a factor of approximately 1.4. Some points of difference pertaining to the flow above the boundary layer include a more distinctive separation between (the lower) $\langle v'v' \rangle$ and (the higher) $\langle w'w' \rangle$, with the ratio being typically 1.1–1.2, and the considerably broader region in which the stresses and turbulence energy are increased, as a consequence of the positive shear strain and thus higher turbulence production occupying a correspondingly wider portion of the flow. Thus, aside from the boundary layer at the lower wall, the distributions of second moments do not contain features not observed in other shear layers. In the boundary layer, the most distinctive feature, also observed previously at $x/h = 2$, is a marked increase of $\langle w'w' \rangle$, and this is again attributed to the splatting effect around reattachment, which causes large pressure fluctuations in combination with convective transport from the reattachment region towards the location being considered. The streamwise stress $-\langle u'u' \rangle$ is observed to develop a local maximum in the boundary layer, but this is mainly due to production associated with the shear strain in the thickening boundary layer – although splatting may, here too, be a contributory process. The simulataneous increase of $-\langle u'u' \rangle$ and $-\langle w'w' \rangle$ in the boundary layer is then responsible for the high level of $-\langle k \rangle$ around $y/h = 0.15$. As the shear stress remains low, for reasons clarified below by reference to the budgets, the ratio $-\langle u'v' \rangle / \langle k \rangle$ reaches very high values, of order 10, well outside the semi-viscous near-wall region.

The budgets for this section are shown in figure 13. In the shear-layer region, the budget for $\langle u'v' \rangle$ is similar to that at $x/h = 2.0$. However, the magnitude of the terms is now considerably smaller, because the velocity gradient and thus production are lower. In contrast to $x/h = 2.0$, turbulent diffusion plays a more important role in balancing production in combination with the more dominant pressure–strain process. The former transports shear stress away from the region of high production towards the wall and the edge of the sheared layer. At this station, production and pressure–strain do not change sign, as would be expected for substantial positive shear straining across the lower flow portion. The pressure–strain contribution develops a near-wall minimum in a region in which pressure diffusion rises and balances the negative turbulence transport and production. Thus the tendency for production to increase the magnitude of the shear stress is counteracted by pressure-related turbulence transport away from the boundary layer, keeping the shear stress relatively low and resulting in the previously observed high levels of the ratio $-\langle u'v' \rangle / -\langle k \rangle$. As the wall is approached through the viscous sublayer, the budget is dictated by a balance between very high pressure–strain and pressure-diffusion contributions. This is a rather surprising observation, but not an unrealistic one, as pressure fluctuations are high in this region and evidently correlate with $\partial u'/\partial y$, which is non-zero at the wall.

The budget for $\langle k \rangle$ shows a significant level of production in the broad shear-layer region, but this is much lower than at $x/h = 2.0$. Also, in contrast to $x/h = 2.0$, it is not much larger than dissipation (the ratio being about 1.2), so that turbulence is here closer to local equilibrium. Alongside dissipation, turbulent transport plays an important role in this layer, transporting turbulence energy away from the region of production towards the wall and the outer region of the sheared flow. Convection also makes an important contribution by transporting high levels of energy from upstream regions (see the budget for $x/h = 2.0$) to the section being considered, thus hindering the approach to turbulence equilibrium. In the boundary layer, the

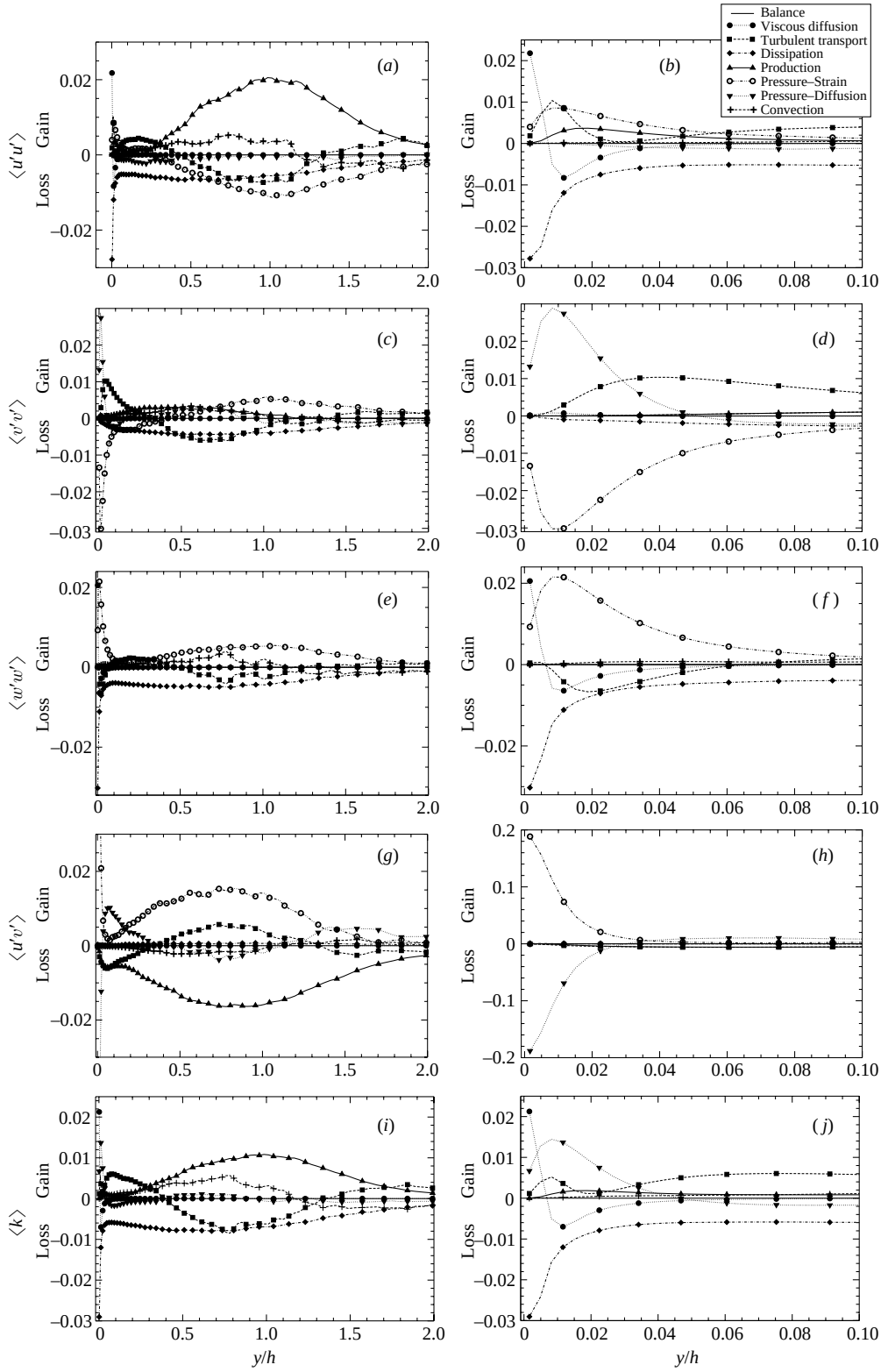

FIGURE 13. Budgets of Reynolds stresses and $\langle k \rangle$ at $x/h = 6$. Left: principal part of the channel, right: zoom onto the bottom wall.

balance is dictated by turbulent transport and dissipation, the former transporting energy from the outer shear layer into the boundary layer. This interaction is very different from that in an ordinary boundary layer bordering an irrotational free stream, in which the balance is mainly between production and dissipation. As the wall is approached, pressure–diffusion is the main opponent of dissipation. As will be shown below, this gain is attained through pressure fluctuations, probably elevated by splatting at the impingement region, being correlated with v-fluctuations. At the wall itself, all terms but viscous diffusion and dissipation tend to vanish, as required by kinematic constraints.

As in the budget for $\langle k \rangle$, the production of $\langle u'u' \rangle$ is now much lower than at $x/h = 2.0$ and so is the pressure–strain term, which here too is the largest sink in the shear-layer region. Also, as in the case of $\langle k \rangle$, convection from upstream regions increases $\langle u'u' \rangle$ and turbulent diffusion decreases the stress by lateral transport away from the central portion of the shear layer. Over most of the boundary layer, $y/h = 0.06 - 0.3$, dissipation is again balanced mainly by turbulent diffusion transporting energy from the shear layer towards the wall. As the wall is approached, pressure–strain rises and, aided by (relatively weak) production, balances dissipation. The positive pressure–strain reflects the need to drain energy from the $\langle v'v' \rangle$ component as turbulence approaches a two-component state by wall blocking, and this energy is transferred to both $\langle u'u' \rangle$ and $\langle w'w' \rangle$. However, the bulk of the pressure–strain-effected transfer will be seen to be to $\langle w'w' \rangle$, and this is probably associated with splatting. At the wall, there is the usual balance between dissipation and viscous diffusion, as is also observed in the budgets for $\langle k \rangle$ and $\langle w'w' \rangle$.

The budget for $\langle v'v' \rangle$ in the shear layer region is dominated by dissipation and turbulent transport which are balanced mainly by a positive pressure–strain contribution, which is derived from $\langle u'u' \rangle$. The most interesting processes pertain to the near-wall region. Here, positive turbulence transport balances the negative pressure–strain contribution, the latter reflecting the process that is required to diminish this component by wall blocking. As the wall is approached, the balance is increasingly dominated by negative pressure–strain and positive pressure–diffusion. Both reflect the high level of pressure fluctuations and the interaction of these with velocity and strain perturbations. It is the high level of pressure–diffusion in the budget of $\langle v'v' \rangle$ which balances the dissipation of $\langle k \rangle$. Importantly, the near-wall dissipation of $\langle v'v' \rangle$ is low and quickly diminishes as the wall is approached, where two-component turbulence leaves little of $\langle v'v' \rangle$ to dissipate. Hence, the near-wall dissipation is highly anisotropic.

The most noteworthy features in the $\langle w'w' \rangle$-budget are again to be found in the near-wall region. Production is necessarily absent, and the near-wall balance is dominated by negative dissipation and a high positive pressure–strain contribution. The strongly preferential transfer of energy from $\langle v'v' \rangle$ to $\langle w'w' \rangle$ is important to highlight, and this is taken to signify the contribution of splatting associated with reattachment, a process that extends over a substantial proportion of the horizontal channel wall. As a consequence of this increase in $\langle w'w' \rangle$, negative turbulent diffusion arises, transporting $\langle w'w' \rangle$ away towards the wall and to the outer part of the boundary layer in which all normal stresses feature positive turbulent transport that supplies the boundary layer with energy from the outer shear layer.

4.6. *Position* $x/h = 8.0$

This position lies in the windward portion of the hill where the flow is subjected to strong acceleration. Profiles of mean velocity and Reynolds stress components in x, y-coordinates are given in figure 10(g, h). Near the lower wall, the angle of the wall

relative to the horizontal axis is about 40°. Hence, u and v are not tangential and normal to the wall, respectively, and this hinders a physically transparent interpretation and discussion. Therefore, in the near-wall region, up to a wall distance of about $0.2h$, profiles of the wall tangential (t) and normal (n) components are also provided in figure 11, albeit not along a line normal to the wall but along a vertical line.

From figure 10(g) it can be seen that the overall behaviour of the u-velocity is similar to that at $x/h = 6$, but due to the acceleration, the velocity is larger near the wall and the boundary layer is thinner (only about $0.05h$). Except near the lower wall, the distribution of Reynolds stresses over the full channel height, as plotted in figure 10(h), is also very similar to that at $x/h = 6$. However, close to the wall, the stresses and the corresponding budgets present some exceptional features not observed at $x/h = 6$, thus meriting closer consideration. As is seen from figures 10(h) and 11(b), one such feature is an extremely high level of spanwise stress $\langle w'w' \rangle$ relative to the normal stresses in the (x, y)-plane. This statement retains its validity whether made in reference to the (x, y) or the (t, n) decomposition. The main difference between the two is that the wall-oriented decomposition highlights the very rapid decay of wall-normal fluctuations, as is expected to occur due to wall blocking. While the stresses in the (x, y)-plane depend on the orientation of the frame of reference, their sum does not, and it is advantageous therefore to consider the distribution of $\langle u'u' + v'v' \rangle/2$ (included in figure 10h) and later also the budget for this quantity, rather than the budgets for the individual components $\langle u'u' \rangle$ and $\langle v'v' \rangle$. For the same reason, the budget for the cross-correlation of u and v, i.e. for the shear stress $-\langle u'v' \rangle$, is not presented here. As seen, $\langle w'w' \rangle$ is also extremely high relative to this sum. Moreover, $\langle k \rangle$ shows a distinct near-wall peak, which is evidently a consequence of the very high near-wall level of $\langle w'w' \rangle$. This extreme behaviour is not observed at other locations, but at $x/h = 7$ (not shown here), $\langle w'w' \rangle$ was already found to exceed $\langle u'u' + v'v' \rangle/2$ very near the wall, indicating that the flow is about to undergo some drastic modification further downstream.

A comparison of the budgets for $\langle w'w' \rangle$ and $\langle u'u' + v'v' \rangle$ at $x/h = 8$ in figure 14 leads to the conclusion that the increase in $\langle w'w' \rangle$ is due to energy being extracted from the latter components and fed to $\langle w'w' \rangle$ by pressure–strain interaction. This is curious, as $\langle w'w' \rangle$ is already higher than $\langle u'u' + v'v' \rangle$, and thus the observation contradicts the usually applied concept of pressure–strain interaction tending to isotropize the normal Reynolds stresses. Hence, models based on this concept must fail here. Interestingly, this mode of transfer – albeit less pronounced – is also observed in the budgets at $x/h = 7$ (not shown here), where pressure–strain is by far the dominant source of $\langle w'w' \rangle$ everywhere. Both $\langle u'u' \rangle$ and $\langle v'v' \rangle$ lose energy through this term. Further upstream, at $x/h = 6$, pressure–strain is also the dominant source of $\langle w'w' \rangle$ close to and further away from the wall. However, close to the wall only $\langle v'v' \rangle$ loses energy while $\langle u'u' \rangle$ gains energy as observed in any flat-plate boundary layer.

Reference to the budget for $\langle w'w' \rangle$ shows production and pressure–diffusion to be zero, as is required by physical constraints. As noted already, pressure–strain is a major source of gain for $\langle w'w' \rangle$. Another is viscous diffusion, the high level of which is consistent with the requirement that viscous turbulence-energy diffusion should balance dissipation at the wall. Away from the wall, viscous diffusion reverses and becomes negative, due to the reversal of the gradient of $\langle w'w' \rangle$. This and turbulence transport largely balance the pressure–strain term and, further from the wall, also the convection contribution.

The loss of $\langle u'u' + v'v' \rangle$ by the action of pressure–strain interaction, seen in figures 14(a) and 14(b), has already been noted. This loss is seen to be largely

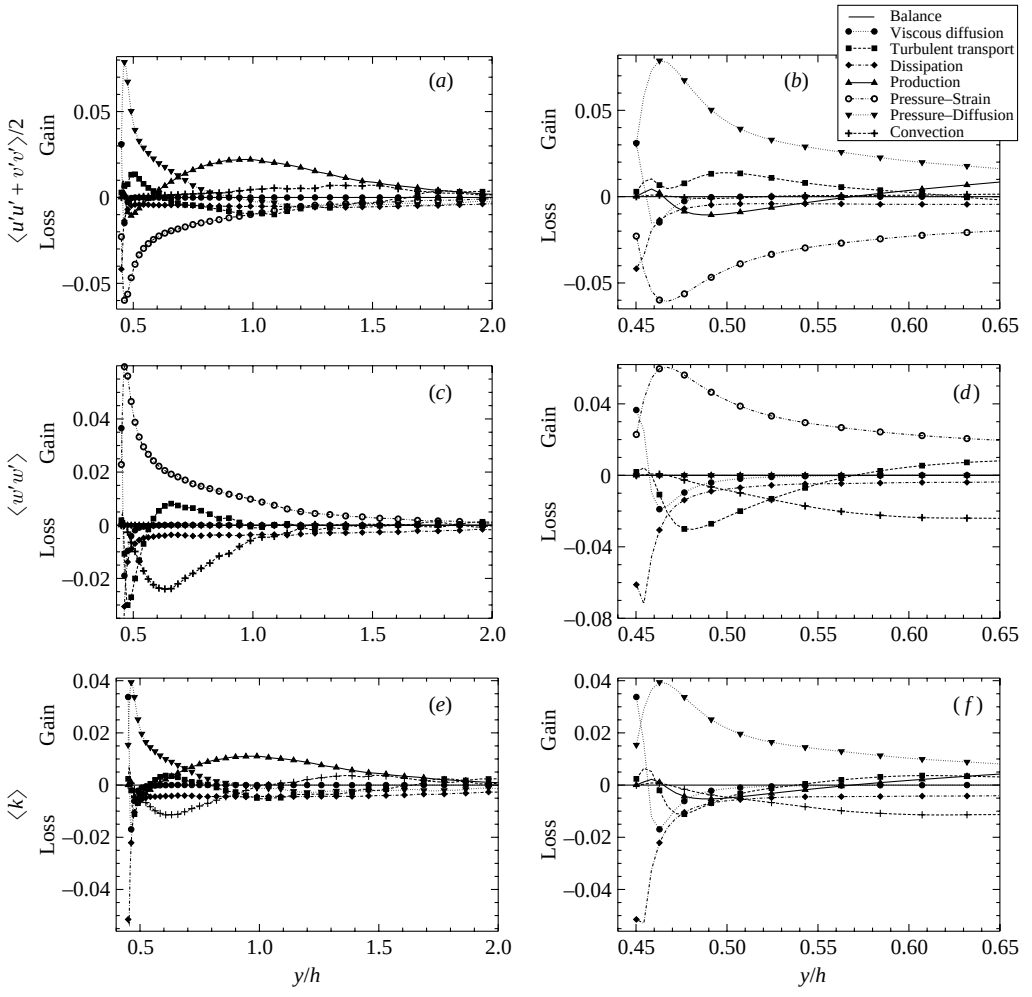

FIGURE 14. Budgets of $\langle u'u' + v'v' \rangle / 2$, $\langle w'w' \rangle$, and $\langle k \rangle$ at $x/h = 8$. Left: principal part of the channel, right: zoom onto the bottom wall.

compensated by pressure–diffusion, except very close to the wall, where the balance is increasingly dominated by dissipation and viscous diffusion, as in the case of $\langle k \rangle$. Thus, here, more than at other locations through the flow, the conclusion that is emerging is that the split of the pressure-fluctuation-containing term into pressure–strain and pressure–diffusion is somewhat synthetic and not necessarily a good basis for constructing closures at second-moment level. It is interesting to observe further that the budgets for $\langle u'u' \rangle$ and $\langle v'v' \rangle$ at $x/h = 8$ display extremely large and opposite levels of pressure–diffusion and pressure–strain, rendering other contributions to the budget almost insignificant. This is quite different to the budgets of the two stresses at $x/h = 6$ and 7, but the difference is due to the Cartesian decomposition relative to the inclined wall at this location. Hence, it is difficult to provide insightful interpretations for these stresses individually, and this is the reason for focusing on their sum in the above discussion.

At this stage it is difficult to provide an unambigous explanation of the precise mechanisms responsible for the anisotropization of the Reynolds stresses at the bottom

wall and the windward face of the hill. Apart from the statistical analysis presented in this section, a detailed analysis of instantaneous structures has been performed and will be presented in the following section. All information available points to the dominance of a splatting effect. This is further supported by the results of Perot & Moin (1995) who investigated near-wall flows with DNS. Their analysis of turbulent budgets near a solid wall without mean flow also features an anisotropization in the budget of the tangential Reynolds stress via the pressure–strain term. To some extent, the present interpretation is also supported by results of simulations of reattaching backward-facing-step flows (Le & Moin 1991; Dejoan & Leschziner 2003), which also feature large spanwise stress levels exceeding the streamwise stress. Here, the effect is perhaps accentuated by the high streamwise velocity in the acceleration region along the windward face of the hill.

4.7. *Anisotropy of the flow*

As argued by Lumley & Newman (1977) and Lumley (1978), the local state of the Reynolds-stress anisotropy,

$$b_{ij} = \frac{\langle u_i' u_j' \rangle}{\langle u_k' u_k' \rangle} - \frac{1}{3}\delta_{ij}. \tag{4.8}$$

may be usefully characterized, in a scalar sense, by the second and third invariants

$$II = -\frac{b_{ij}b_{ij}}{2}, \quad III = \frac{b_{ij}b_{jk}b_{ki}}{3}. \tag{4.9}$$

Because the trace b_{ii} vanishes, these two invariants are the only independent scalar norms associated with b_{ij}. Since departure from isotropy appears as a second-order effect in a (III, II)–diagram, it is often preferred to identify the anisotropy by

$$\xi = \left(\frac{III}{2}\right)^{1/3}, \quad \eta = \left(-\frac{II}{3}\right)^{1/2} \tag{4.10}$$

(Pope 2000). All realizable (physically realistic) states of turbulence lie within the triangular domain in the (ξ, η)-plane, shown in figure 15. The upper line corresponds to two-component turbulence, the left-hand line to 'axisymmetric contraction' and the right-hand line to 'axisymmetric expansion'. This terminology is linked, formally, to the shape of the Reynolds-stress ellipsoid, the length of its principal axes being dictated by the eigenvalues of the Reynolds-stress tensor.

A useful third norm, proposed by Lumley, combines II and III to form the 'flatness parameter'

$$A = 1 + 9(III + II). \tag{4.11}$$

In isotropic turbulence, both invariants vanish, in which case $A = 1$. The other extreme condition is two-component turbulence – say at a wall or sharp fluid–fluid interface – where $II = -III - 1/9$ so that $A = 0$.

The value of the above representation lies in its usefulness to turbulence modellers attempting to construct improved anisotropy-resolving closures. Such closures, especially at second-moment level, make use of the above invariants to secure the correct behaviour in limiting (homogeneous) flow states and flow configurations. For example, observations for fully developed channel flow, derived from experiments and DNS, show that a traverse from the channel centreline towards the wall corresponds to a characteristic path in the Lumley triangle, starting in the vicinity of $\xi = \eta = 0$ (isotropy), progressing along the 'axisymmetric expansion' line (in the log-law region) and ending in the upper portion of the 'two-component-turbulence' line.

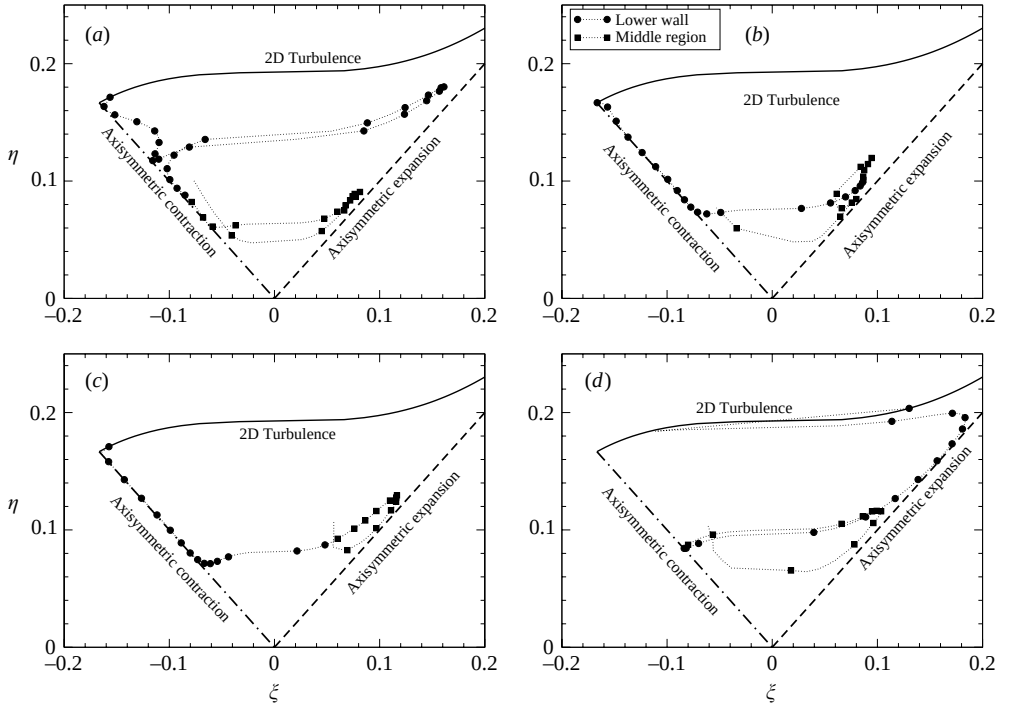

FIGURE 15. Invariant maps along vertical lines at four streamwise locations: (*a*) $x/h = 0.5$, (*b*) $x/h = 2.0$, (*c*) $x/h = 6.0$, (*d*) $x/h = 8.0$. The line partly outside the triangle at the upper boundary in (*d*) is an artefact resulting from the connection of two points far apart.

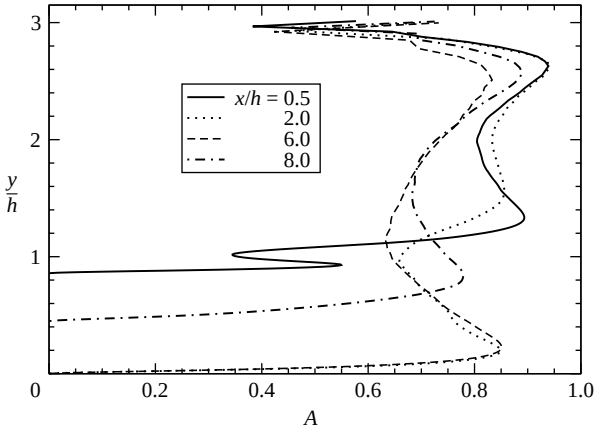

FIGURE 16. Distribution of the flatness parameter A at different streamwise locations, $x/h = 0.5, 2.0, 6.0, 8.0$.

Figure 15 shows the loci associated with traverses across four streamwise locations, while figure 16 gives corresponding profiles of the flatness parameter A (profiles of II and III can be found in Jang *et al.* (2002)). The traverses in figure 15 stop short of the layer closest to the upper wall, as the turbulence structure is not well resolved in this region. A first observation is that all states indeed lie within the triangle, as is required by realisability constraints. In the central region of the channel, covering 80% of the

flow and identified by the solid squares, the flow is moderately anisotropic, as is also identified by the value of A being around 0.8. Excluding the 10% near-wall layer, any deviations from this state occur close to the axisymmetric-expansion line and correspond, broadly, to the behaviour observed in the log-region of a channel flow. As the region close to the lower wall is traversed, turbulence is seen to approach the two-component state at all four locations. However, the manner in which this approach takes place varies greatly. Within the separation zone and marginally beyond the reattachment point, the approach occurs mostly along the 'axisymmetric contraction' line, signifying a state very different from that in a log-law layer. An exceptional excursion occurs, however, at $x/h = 0.5$, and this corresponds to the sharp dip in A at around $y/h = 1$ (figure 16). To appreciate the origin of this feature, attention needs to be directed to the map for $x/h = 8$. In this, the $\xi - \eta$ locus covering the near-wall layer shows a trend towards that characteristic of a log-law region, reflecting the partial recovery of the flow allowed by the distance between reattachment and the following hill. The state of the near-wall layer around $x/h = 0$ is closely linked to that at $x/h = 8$. The flow then separates slightly further downstream, and at $x/h = 0.5$ it contains the separated shear layer that is associated with the attached boundary layer just upstream of that location. Thus, the excursion at $x/h = 0.5$ appears to be the footprint of the attached boundary layer prior to separation.

The proximity of the ξ–η locus to the axisymmetric contraction line, especially at sections $x/h = 2$ and 6, is reminiscent of that seen in a developed free shear layer (Bell & Mehta 1990). While the present near-wall flow is clearly not a shear layer, it is akin to a wall jet which combines a thin boundary layer with a much thicker outer free shear layer that is only weakly affected by the wall. This equivalence, albeit qualitative, thus provides an explanation for the behaviour observed in figure 15. A point of difference is, however, that the anisotropy in a free shear layer is considerably lower than that in a near-wall layer, so that the former never approaches the two-component state. In the present case, in contrast, the backward-moving shear flow in the recirculation region behaves like a thin boundary layer as the wall is approached, and thus the flow structure has to approach the two-component limit at the wall.

5. Analysis of spectra

5.1. *Spectra in the interiour of the flow, general assessment*

Time signals of velocity have been recorded in RUN 2 on a dense set of points spread over the domain. The length of the data set in time is 33.25 non-dimensional units ($t_{ref} = h/U_b$), corresponding to 29 596 time steps or 3.7 times the nominal flow-through time L_x/U_b. Using the smaller bulk velocity between the hills yields about 2.5 flow-through times. The time signals were recorded over a duration shorter than the total averaging (performed within the computation itself) for reasons of economy. No time signals are available from RUN 1.

The analysis was performed using a windowed Fourier transform with a Hann window (Press *et al.* 1992) and segments of length 2^{14} samples, i.e. spanning a length of 18.4 time units. The full signal was decomposed into four such overlapping segments over which averaging was performed. Furthermore, signals were recorded for each (x, y) position at 11 different z-locations over which additional averaging was performed. These parameters were selected so as to obtain the best possible compromise between smoothness of the spectrum and width of the frequency window covered. Figure 7 shows the points where spectra were computed. They were chosen so as to

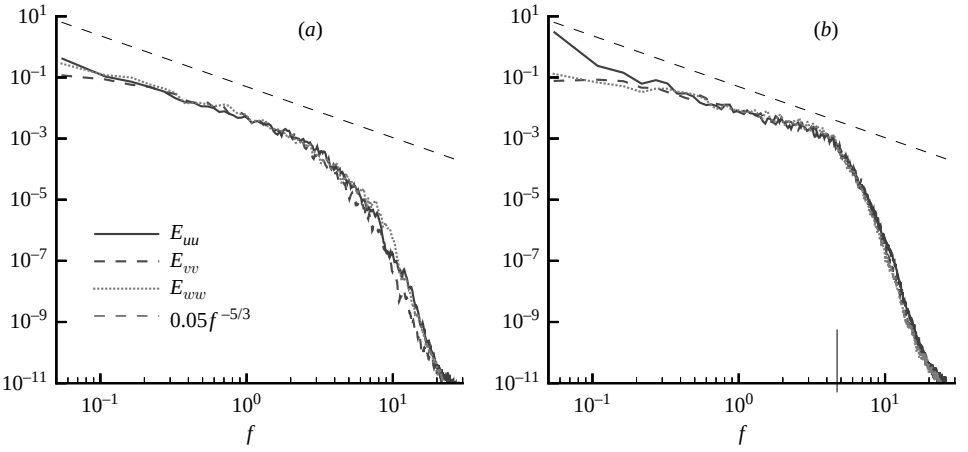

FIGURE 17. Power spectrum density of one-dimensional spectra of the three velocity components: (*a*) in the centre of the recirculation zone at $x/h = 2.15$, $y/h = 0.49$, (*b*) in the centre of the shear layer at $x/h = 2.23$, $y/h = 1.13$ (see figure 7). The dashed line has a slope of $f^{-5/3}$. The small vertical line in (*b*) is at $f_{CDS} = 4.7$ as discussed in the text.

cover all characteristic areas in the flow, but only the most relevant ones are discussed in this section.

Attention is first focused on the issue of numerical resolution, some aspects of which have already been considered in § 3.3.3. Figure 17 shows the power-spectrum density at two points with different characteristics. Both spectra were recorded around $x/h = 2$, one in the centre of the recirculation region and the other in the shear layer. For the former $\langle u \rangle \approx \langle v \rangle \approx 0$, whereas $\langle u \rangle = 0.73$ for the latter. These spectra exhibit several distinct ranges: low frequencies around the inverse of the flow-through time, i.e. around 0.1, a middle region of regular decay, and a high-frequency region of faster decay. Checks were performed to verify that, except for some near-wall spectra discussed below, all other spectra computed at the points shown in figure 7 have characteristics between the two extremes displayed in figure 17. All components show the same spectrum, reflecting an isotropic distribution of spectral energy, except at very low frequency.

In the spectrum of figure 17(*a*), a regular decay of slope close to $-5/3$ is observed over more than one decade in f. This is indicative of an inertial subrange, a necessary condition for the flow to behave like locally isotropic turbulence. For higher frequencies, a smooth transition to a faster decay is observed, related to the effective filter of the LES. The present spectra are spectra in time. They can be related in most circumstances to spectra in space by means of Taylor's hypothesis. However, this requires the average velocity to be substantially larger than the fluctuations which is not the case for the particular point under consideration in the centre of the recirculation zone.

The second spectrum, figure 17(*b*), exhibits the same type of ranges discussed above. In contrast, however, a pronounced change of slope is observed at $f = 4.7$. This can be explained by the characteristics of the second-order central scheme employed for the convective term. The scheme has a modified wavenumber $\xi_{eff} = \sin(\pi\xi/\xi_{max})$ in space, exhibiting a maximum at $\xi_{max}/2 = 1/(4\Delta_x)$ (Ferziger & Peric 1996). Any contribution with spatial wavenumber larger than this value is not adequately transported in space. Employing Taylor's hypothesis for this point is possible, subject to uncertainty arising from the relatively low mean velocity, $\langle u \rangle / \langle u'u' \rangle^{1/2} \approx 3$ where the signal was recorded.

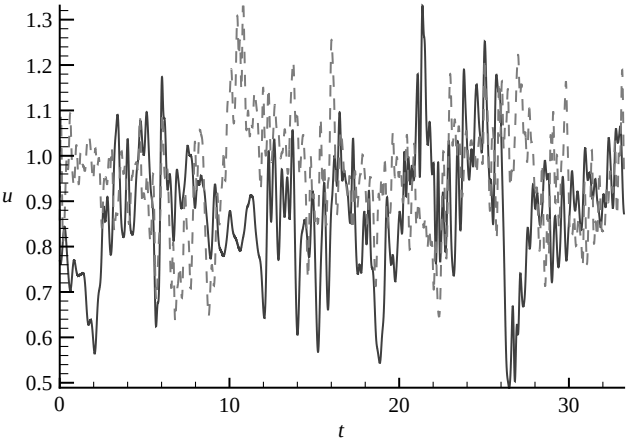

FIGURE 18. Two u-signals in the outer flow at $y/h = 2$ and the same z-location, one at $x/h = 2.2$ (dashed line), the other at $x/h = 8.0$ (solid line).

Hence, the critical frequency in time is $f_{CDS} = \langle u \rangle / (4\Delta_x)$, which is 4.7, indicated by the short vertical line on the graph in figure 17(b). The physically meaningful range of this spectrum therefore extends up to f_{CDS}. Similar observations were made by Schmitt, Richter & Friedrich (1986). An approximate relationship to the Kolmogorov length discussed before can be established by observing that the maximum resolvable spatial wavelength at the present point generates the temporal frequency $f_\Delta = \langle u \rangle / (2\Delta_x)$ and $\Delta/\eta \approx 10$. The temporal frequency related to η would then be around 94. Note that these considerations are not applicable to the spectrum in figure 17(a) because $\langle u \rangle \approx \langle v \rangle \approx 0$.

The most important criterion for assessing the quality of resolution in a simulation is the ratio between the energy content of the most energetic modes and the ones with the highest physically meaningful frequency. In the present simulation, this is about two decades in the most critical area near the crest of the hill, indicative of a good resolution by the grid and method employed.

Attention is turned next to the low frequencies in the spectra. Two representative time signals are given in figure 18. These were recorded in the outer flow at a streamwise distance of $6h$ on the same average streamline and at the same spanwise position. Low-frequency undulations are visible in these signals. Animations of the whole flow field show that, at certain instances, turbulent fluctuations 'accumulate' in some regions before they are 'swept' away. The two-point correlation coefficient R_{11} between the two u-signals considered is only -0.085. Similar values were observed at other locations. This indicates that the strong fluctuations are of substantially smaller size than the distance between these points. The low frequencies of around 0.1 are therefore principally due to the return time of the periodic flow, as illustrated by the limiting case of frozen turbulence advected in a plane channel. The length L_x of the domain in the streamwise direction is therefore sufficient, because the size of the dominating vortex structures in space is substantially smaller than L_x.

5.2. *Spectra for near-wall points*

By means of the spectra in figure 19, further insight can be gained into the anisotropy in the Reynolds stresses observed close to the wall at $x/h = 8$. The figure shows spectra at four near-wall locations, at about $x/h = 0, 4.5, 6, 8$ and a distance of $0.09, \ldots, 0.1h$ from the wall. The fourth was selected to be somewhat closer to the wall, at a

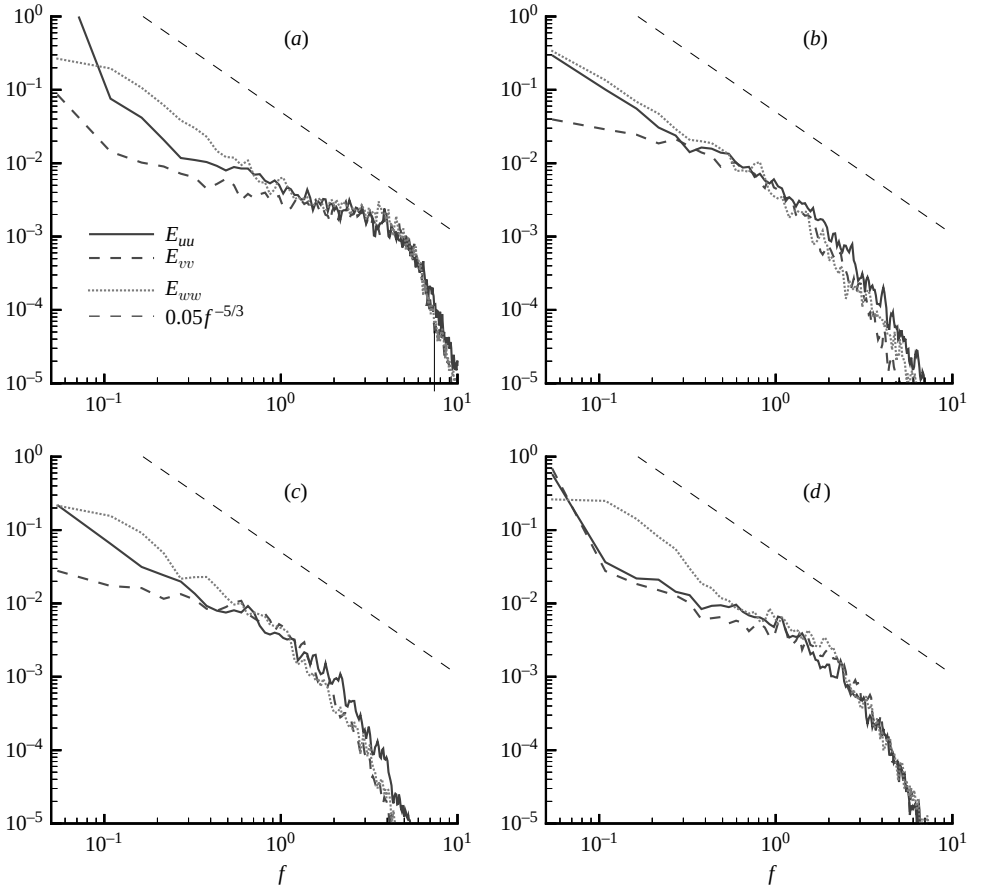

FIGURE 19. Power spectrum densities at several near-wall locations: (*a*) $x/h = 0$, (*b*) $x/h = 4.5$, (*c*) $x/h = 6.0$, (*d*) $x/h = 8.1$ (see figure 7). The distance from the wall is $0.09h$–$0.1h$ for the first three and about $0.06h$ for the fourth. The dashed line has a slope of $f^{-5/3}$.

wall-normal distance of $0.06h$, because of the reduced thickness of the boundary layer at this location. The limiting frequency f_{CDS} is relevant only for the first of these spectra, for which $\langle u \rangle \approx 1$. At the other points the streamwise velocity is substantially lower.

Figure 19 shows that all temporal fluctuations with frequency larger than 1 feature similar, isotropic decay in their power spectra. The most interesting range is that containing the low frequencies. At $x/h = 4.5$, these components are large for u and w, and small for v, with equal energy in u and w. Further downstream, at $x/h = 6$ and $x/h = 8$, a substantial level of anisotropy gradually develops for frequencies in the decade $f = 0.06$–0.6. The energy content in the w-fluctuations increases substantially compared to the other two components, reaching a ratio of up to 10 at $x/h = 8$ for $f = 0.1$. The anomaly in the spectrum persists until the crest of the hill, which is revealed by the corresponding spectrum for $x/h = 0$. Due to the pronounced acceleration, the energy in the u-component increases as the flow progresses from $x/h = 8$ to 0, while w and especially v diminish. Downstream of the crest, the dominance of the w-fluctuations in the low-frequency range is reduced substantially, as is revealed by the spectra at around $x/h = 2$ in the shear layer shown in figure 17. The

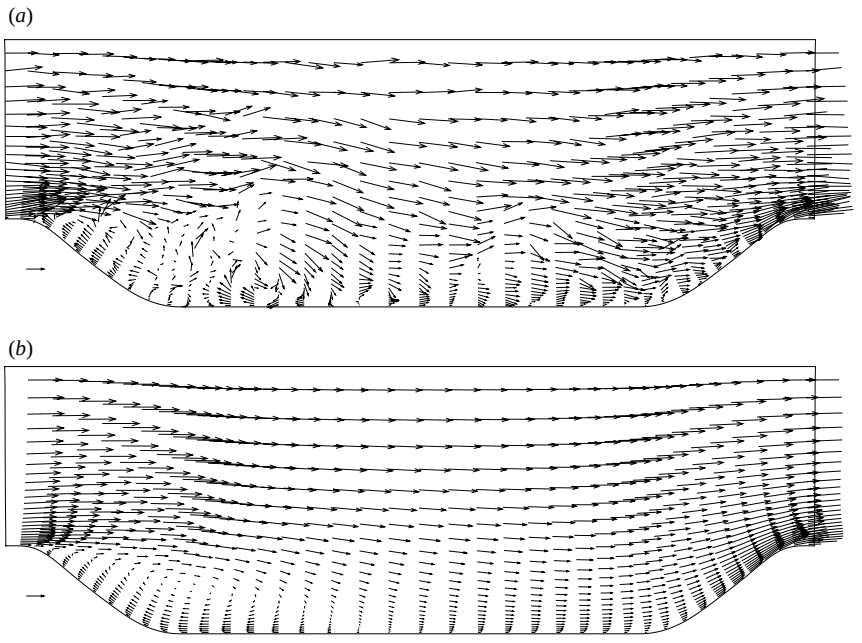

FIGURE 20. Vector plots in a vertical plane aligned with the x-direction: (a) instantaneous flow, (b) average flow. An arrow is shown at every fifth grid point, horizontally and vertically.

near-wall spectra at this x-position (not included here) also exhibit this reduction. These observations support the earlier discussion. Furthermore, the spectra show that the dominance of w-fluctuations is a comparatively slow effect. It is related to temporal periods of, typically, 5 to 10 time units.

6. Analysis of instantaneous flow structures

6.1. *Unsteadiness of the flow*

In this section information is provided about the instantaneous flow and its complex physical behaviour in terms of structural features. This allows an explanation of certain observations made earlier in the discussion of statistically averaged quantities. The vortex structures in different flow regions will be described with reference to several instantaneous quantities, which were derived from RUN 1.

First, two plots of velocity vectors in a vertical plane are shown in figure 20, part (a) being an instantaneous snapshot and part (b) representing the time-averaged field. The comparison conveys an impression of the large-scale dynamics at play and the high level of turbulence which is clearly different from what was found in the computations for low-Reynolds-number flow over wavy-wall geometries (Calhoun & Street 2001; Zedler & Street 2001). The unsteady activity is especially pronounced in the recirculation region and at the windward foot of the hill. The intense irregularity of the flow presents a substantial challenge to its analysis and the extraction of ordered structures. In the reattachment region, as well as along the windward slope of the hill, a substantial portion of high-velocity fluid is directed towards the wall, an observation revisited later. The vector plot of the average flow illustrates well the strong acceleration along the windward slope of the hill, resulting in a very thin boundary layer and a velocity overshoot near the crest.

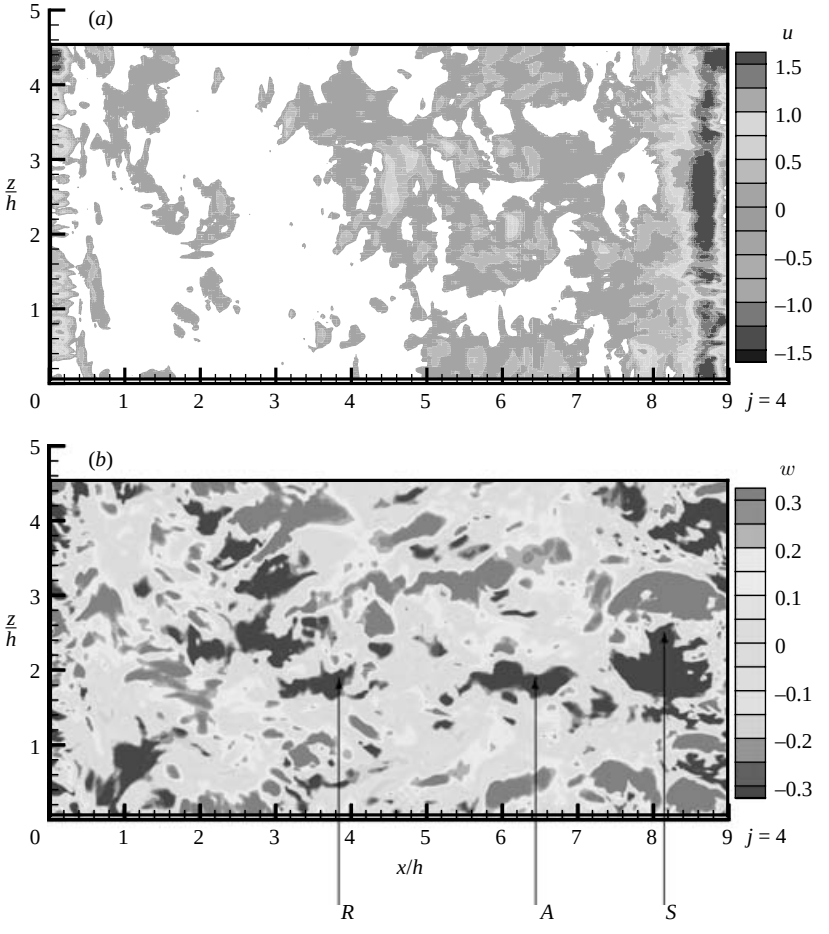

FIGURE 21. Typical snapshots of the instantaneous velocity near the bottom wall, values taken at the fourth grid point from the wall: (*a*) streamwise velocity component with all negative values being removed, (*b*) spanwise velocity component.

The high irregularity of the flow manifests itself also in large variations of separation and reattachment loci. In fact, the concept of a single line of separation or reattachment, while pertinent to the average flow, is not meaningful for the instantaneous flow separating from a smooth wall (Na & Moin 1998). This is demonstrated by the plot in figure 21(*a*) which shows an instantaneous picture of the streamwise velocity very close to the bottom wall. The removal of negative values from the data shows that forward and backward flow occur in a spotty manner. Instantaneous forward flow appears in the recirculation region and substantial backflow is observed well beyond the average reattachment point – in fact, almost everywhere in the domain except on the upper half of the hill's windward face. A reattachment 'line' cannot be identified as such. Animations reveal that the locations of forward and backward flow also change in highly irregular fashion in time. Instantaneous separation is confined to a smaller region than reattachment, due to the convex wall curvature, but still occurs over a distance of $-0.1 \lesssim x/h \lesssim 0.7$. A statistical quantification was obtained by evaluating an intermittency coefficient, here defined as the temporal percentage of time at which the u-velocity is negative. Within the recirculation zone, close to the

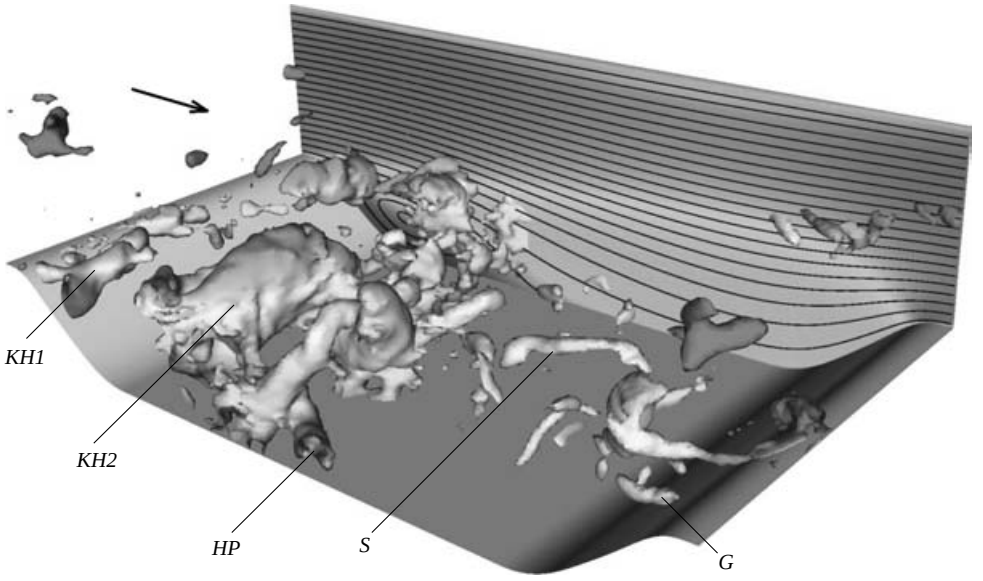

FIGURE 22. Instantaneous iso-surface of the pressure perturbation p'.

wall, its value varies from 90% at $x/h = 3$ to around 50% at the hill cest and the nominal reattachment location and vanishes at the windward face of the hill beyond $x/h = 8.4$ before again increasing towards the crest.

6.2. *Vortex systems*

Figure 22 shows a three-dimensional iso-surface plot of the instantaneous pressure fluctuations p'. Pressure fluctuations were found to be better suited than the pressure itself to elucidate structures, because the spatially variable mean pressure tends to obscure structures in certain regions. Animations have been created to support the interpretation presented below.

In the shear layer downstream of the crest of the hill, spanwise vortices are observed, which are generated through Kelvin–Helmholtz instability (label KH1). While these vortices have a size of the order of the boundary-layer thickness at the crest of the hill, they rapidly grow until they reach a diameter of about one hill height (label KH2). On the other hand, figure 22 shows that these 'rollers' do not extend over the whole spanwise domain. First, their formation does not take place uniformly, since the flow at the separation point is turbulent, with streamwise vortices swept over the crest of the hill contributing to their disruption. Second, these vortices break up further downstream due to secondary instabilities, a feature which is commonly observed in bluff-body flows, e.g. around cylinders (Zdravkovich 1997). This process is related to the generation of streamwise vorticity and streamwise elongated structures which are inclined with respect to the x-axis in vertical direction, as revealed by the w-fluctuations shown in figure 23(b). These structures are frequently 'trapped' in the recirculation zone and swept back to the separating shear layer, where they can trigger irregularities in the separation and roll-up process. Another type of vortex (labelled HP in figure 22) appears occasionally between the major Kelvin–Helmholtz rollers. Pictures of p'-iso-surfaces, as in figure 22, but viewed from above (not included here), support observations derived from plots such as figure 22, namely that these vortices are inclined with respect to the x-axis, but horizontally in preference. They are related

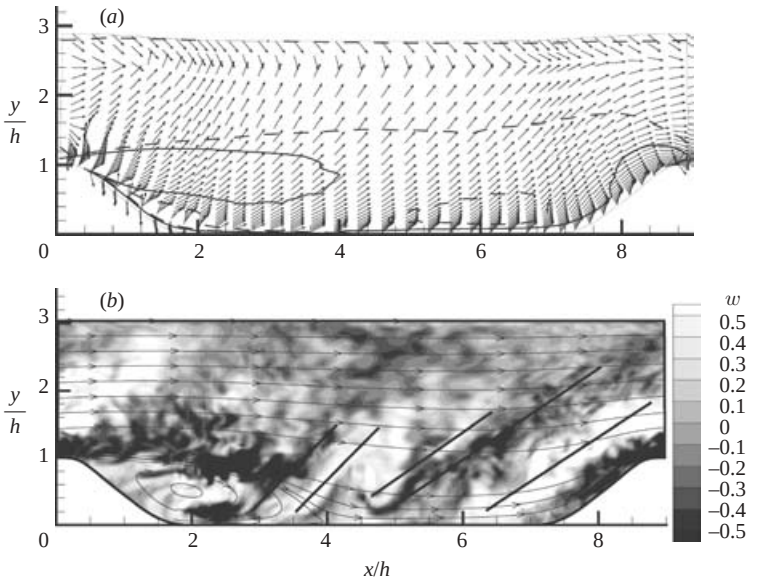

FIGURE 23. Generation of inclined vortex structures. (*a*) Average deformation determined by the principal axes of the average deformation tensor. Represented is the direction of the first eigenvector related to local stretching, the length is unity. Contour lines have been placed at $\sigma_1 = 0.05$ (dashed) and $\sigma_1 = 0.1$ (solid). (*b*) Instantaneous spanwise fluctuations in a vertical plane. The range has been reduced from ± 1.3, comprising the extrema, to ± 0.5 and straight lines have been introduced to enhance visibility.

to a helical pairing of the principal spanwise vortices and are, in fact, commonly observed in mixing layers or in the flow behind a backward-facing step (Silveira-Neto *et al.* 1993). Further downstream, in the reattachment region, the core flow is quite irregular, but occasionally exhibits streamwise vortices like the one labelled S in figure 22. In the windward region of the hill, the wall is concave, which makes the flow prone to the development of streamwise vortices due to the Görtler instability. Indeed, vortices of this type are observed in the present case (labelled G in figure 22), but another interpretation is possible as discussed below.

Through secondary instabilities, the spanwise Kelvin–Helmholtz-type vortices in the shear layer yield streamwise vortices as indicated above. Further downstream, their preferential orientation is in x-direction, but they are inclined in the vertical direction as revealed in figure 23(*b*) by way of instantaneous w-fluctuations. Beyond $x/h \approx 3$, these structures still evolve, mainly due to the action of the mean velocity. The latter exhibits a strong vertical gradient, as illustrated by the vector plot in figure 20 and the profiles in figure 10. This is related to a pronounced average spanwise vorticity of the same sign across the flow domain, except in the vicinity of the upper wall. As a consequence, the streamwise structures, highlighted in figure 23(*b*) by straight lines, exhibit a tendency to turn in a clockwise direction. During this process, their lower end is retained in the low-speed region and can even be transported in the upstream direction by the recirculating flow. As for any flow, the two-dimensional average flow can be decomposed into translation, rotation (just discussed), and deformation. The deformation introduced by the mean flow is highlighted in figure 23(*a*) using the principal axes of the average deformation tensor (Wu & Durbin 2001). Both eigenvectors are orthogonal and the corresponding eigenvalues are of the same

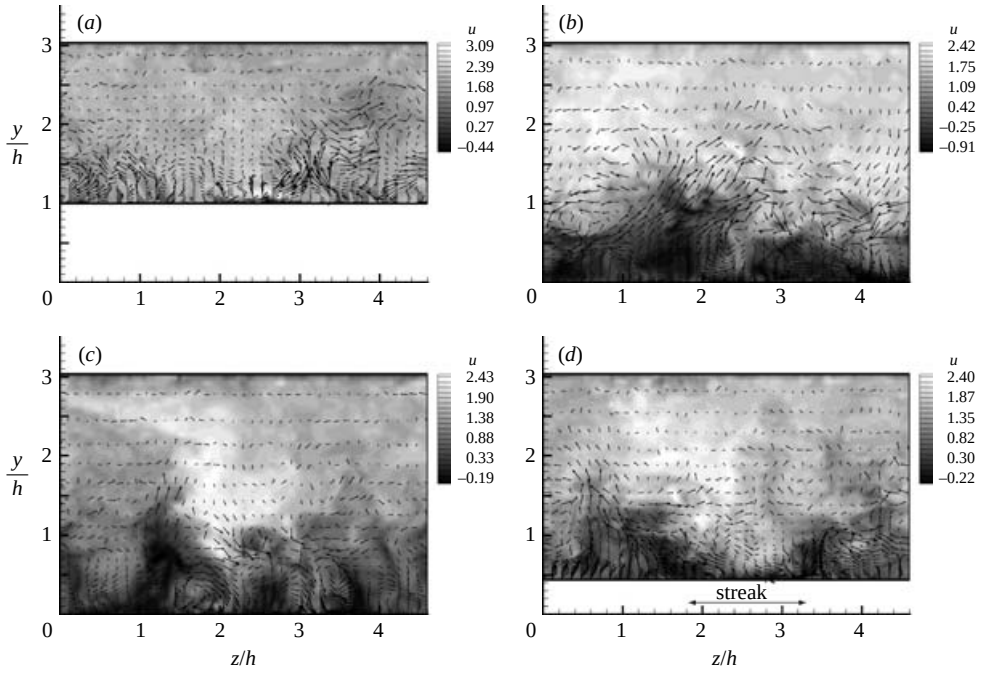

FIGURE 24. Instantaneous velocity in planes of the grid with constant streamwise index i: (*a*) $x/h=0.05$, (*b*) $x/h=2$, (*c*) $x/h=6$, (*d*) $x/h=8$ where equality holds approximately only due to the inclinations of the grid lines in vertical direction. Vectors are composed of the instantaneous v- and w-components. They are located at every fifth grid point in the horizontal and vertical directions, respectively. The grey scale shows the streamwise velocity with levels adjusted to the extrema in the respective slice.

magnitude but opposite sign due to continuity. The vectors in figure 23(*a*) have unit length and point in the direction of the first eigenvector, related to the positive eigenvalue and hence local stretching. Compression by the same amount is applied in the orthogonal direction so that the second eigenvector field need not be displayed here. Two contours in this picture indicate where the first eigenvalue, σ_1, is larger than 0.05 and 0.1, respectively. The latter covers mainly the separating shear layer and the region just ahead of and along the windward face of hill. Hence, while transported downstream, the inclined structures are stretched in longitudinal direction.

The process of rotation and stretching has important consequences for vortices not already aligned with the principal axes of the average deformation tensor. It has been observed, in animations of iso-p' surfaces, e.g., that vortices of predominantly spanwise orientation, with one end slightly lower than the other, are turned to become oriented according to the axis of average stretching. This is the reason for the preferrential orientation of vortices observed over the downstream half of the domain.

6.3. *Streamwise structures*

As a result of the mechanism described above, streamwise structures (identified through w-fluctuations) are observed at the bottom wall, which are the footprints of those in the interior of the domain. They are visible in figure 21(*b*) in both the recirculation and post-reattachment region and examples are labeled *R* and *A*, respectively. Figure 24 provides further information on the near-wall streamwise structures. It shows snapshots of instantaneous velocity in nearly vertical grid planes (planes with

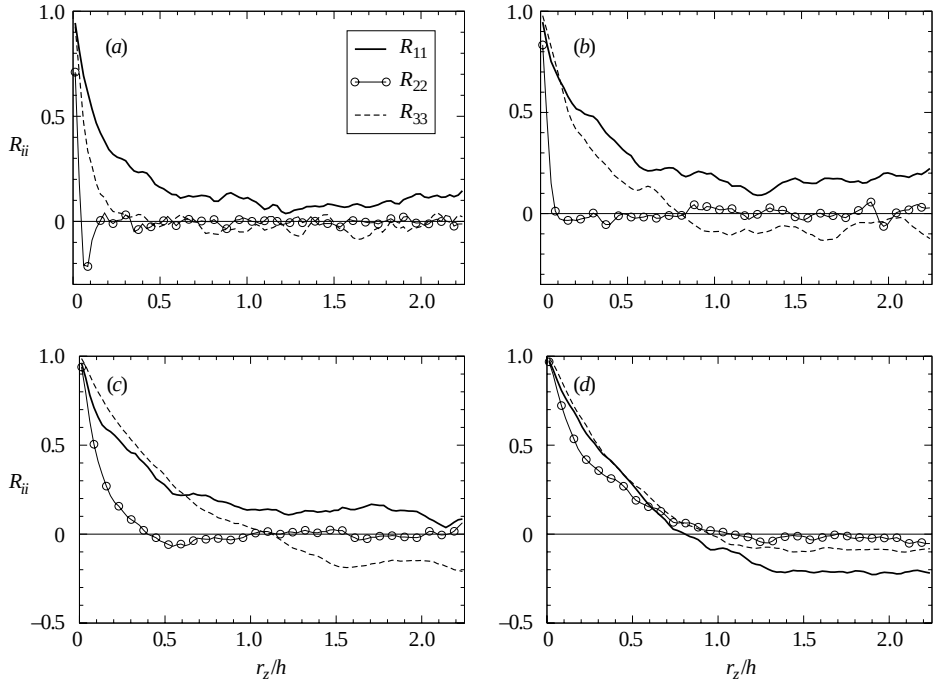

FIGURE 25. Spanwise auto-correlation functions at $x/h = 6$, obtained from RUN 2 over a period of 33 non-dimensional time units and four distances from the wall: (*a*) $y/h = 0.00161$, (*b*) $y/h = 0.02247$, (*c*) $y/h = 0.2179$, (*d*) $y/h = 1.01$. The curves represent the correlations of the u-fluctuations, R_{11}, of the v-fluctuations, R_{22}, and of the w-fluctuations, R_{33}, respectively, as a function of the spanwise separation r_z/h.

constant streamwise index i). The grey scale represents the streamwise velocity component. In the plot for $x/h = 2$, located in the recirculation zone, ordered structures can hardly be discerned, although pressure surfaces show that the velocity field is far from random. In the plot for $x/h = 6$, several high- and low-speed regions are observed, and the vectors show vortical structures. These are confined to the trough, i.e. to $y/h = 0$–1 and have a width of about $0.5h$–$1h$. In order to convey this in quantitative terms, correlation coefficients of all velocity components have been computed as a function of the spanwise separation r_z/h at $x/h = 6$ and at four distances from the wall. These are given in figure 25. Plots (*a–c*) are for the near-wall flow, up to $y/h = 0.22$. In these, the correlation length for the wall-normal velocity v is substantially smaller than those for the other velocity components, as revealed by the faster decay near the origin and the zero crossing at low r_z/h values. The correlation of the u-component near the wall is substantially larger than that of the other components, and coherence increases with wall distance. The correlation of the w-fluctuations, on the other hand, is small at the wall but increases above it such that a variation similar to that of the u-fluctuations is observed at $y/h = 0.22$.

Consideration is next given to the region at hill height and above. The inclined structures in figure 23 typically extend up to about $x/h = 2$, and hence should have an impact in this region away from the wall. The structures even extend well above the hill crest, as seen in figure 23. At low Reynolds numbers, Street and coworkers (Calhoun & Street 2001; Zedler & Street 2001) show pronounced streamwise vortices over the crests of the hills in the 'wavy-terrain' configuration. Salvetti *et al.* (2001) find,

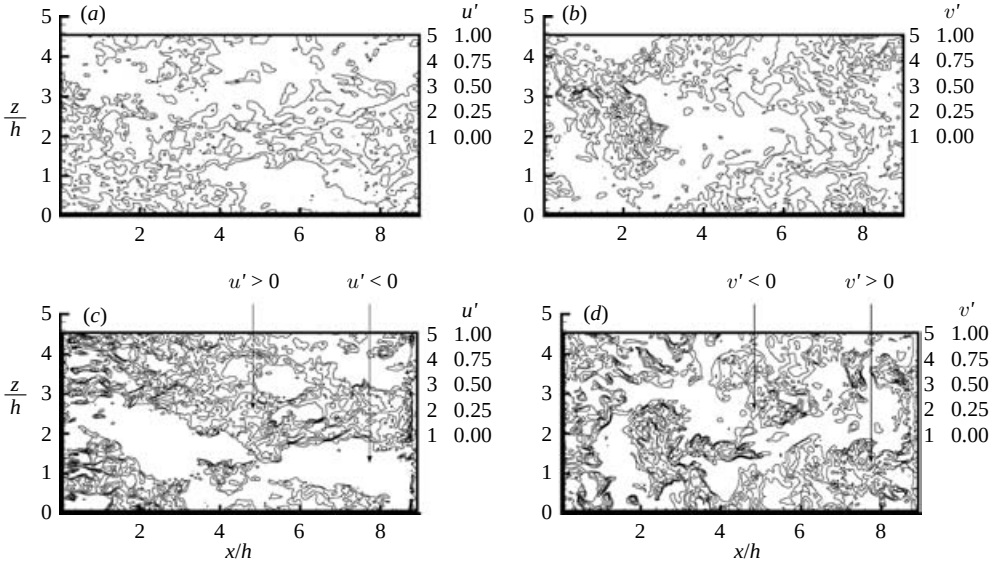

FIGURE 26. Instantaneous fluctuations in horizontal planes $y/h = 2$ (a, b) and $y/h = 1$ (c, d). Left (a, c): streamwise fluctuations u', Right (b, d): normal fluctuations v' for the same instant. To enhance clarity, negative values have been discarded.

at a higher Reynolds number, similar structures in this configuration when considering the normal fluctuations v' in horizontal planes at about one half of a hill height over the top of the hill crest. In fact, such observations were first made by Gong *et al.* (1996) and explained as being a cosequence of a Craik–Leibovich type-2 instability (Phillips & Wu 1994; Phillips, Wu & Lumley 1996). To investigate whether similar structures arise in the present geometry, instantaneous data were extracted across several planes at constant y values. Figure 26 shows a plot of v' at $y/h = 1$ (hence touching the hill crest) and at $y/h = 2$. The plotting style is similar to the one used in Gong *et al.* (1996) and Salvetti *et al.* (2001), so that a qualitative comparison with these results for a sinusoidal bottom wall is possible. The corresponding u'-fluctuations are also included in figure 26. The latter exhibit large streamwise structures which become evident when negative contours are suppressed. The v' fluctuations do not show the same pronounced streaky behaviour as in Gong *et al.* (1996) and Salvetti *et al.* (2001), but are substantially more irregular. Comparing u' and v' in figure 26 suggests that positive v' is correlated with negative u' which is especially evident along the windward slope of the hill at $x/h \approx 6$–8. Arrows to sample structures have been inserted to make the correspondence more visible. This correlation is substantiated by the Reynolds stresses displayed in figure 10. Based on these data, the one-point correlation coefficient R_{uv} has been computed. It is negative and its magnitude is larger than 0.4 for $y/h = 0.4$–2.1 at $x/h = 6$, and for $y/h = 0.8$–2 at $x/h = 8$, for example. In plots similar to the ones in figure 26, but obtained closer to the wall (not included here), the structures seen in figure 26 persist but become shorter and narrower, increasingly resembling the view of the near-wall region provided by figure 21. Further away from the wall, for $y/h > 1$, the fluctuations become increasingly attenuated, as revealed by the plots at $y/h = 2$ in figure 26 and the statistical data in figure 10. To some extent, the streaky patterns can still be perceived in these plots. In comparison to the results of Salvetti *et al.* (2001), obtained at a Reynolds number similar to the

present one, it is thus found that, for the present substantially larger distance between consecutive constrictions and because of the lower channel height, the generation of streamwise structures in the outer region above the hill crest is considerably reduced.

The streamwise structures away from the bottom wall can also be recognized in figure 24. The snapshot at $x/h = 2$ does not reveal a particular organization, but the fluctuations in the shear layer are quite vigorous. At $x/h = 6$ and 8, an area of positive u-fluctuations, occupying about one third of the domain, can be observed. The spanwise correlations at $x/h = 6$, $y/h = 1$ in figure 25 address this issue in an average sense. The correlations of the v-fluctuations, R_{22}, level off to zero around $r_z/h = 1$, and R_{33} behaves in a similar manner, being somewhat larger near the origin. The u-correlation, R_{11}, equals R_{33} until $r_z/h \approx 0.7$ and shows negative values of about -0.2 for large r_z/h. Hence, the correlations of the u-fluctuations are increased over a larger distance than those of the other components, while the fluctuations themselves are about twice as intense, as revealed by the Reynolds stresses in figure 10(f).

At the time of completing the present manuscript, a study by Günther & von Rohr (2003) reported streamwise u-velocity streaks above the hill crests in experiments on a wavy wall at $Re_h = 7300$ and $\lambda/h = 10$. These results thus also support the present findings. The spanwise period of the u-fluctuations in Günther & von Rohr (2003) is $1.5\lambda = 15h$, which is substantially larger than observed here. However, their measurements were conducted with a distance of $9.5h$ between the hill crest and the upper wall, in contrast to $2.05h$ in the present case. It is as yet unknown how this parameter influences the size of these structures, but some scaling involving the channel height must be expected.

6.4. *Structures near the windward face*

The analysis of the Reynolds stresses at $x/h = 8$ in figure 10(h) and figure 11(b) and their budgets in figure 14 revealed the dominance of fluctuations in the spanwise direction associated with the transfer of energy to this component by the pressure–strain term. First signs of this process can already be observed at $x/h = 6$, where the pressure–strain term Φ_{33} dominates around $y/h = 0.01$ (see figure 13f), which is accentuated at $x/h = 7$ (budget not shown here) and becomes substantially stronger at $x/h = 8$ (figure 14d). To further elucidate this process, attention is focused on the instantaneous flow structures in this region. This has been done by animations of p- and p'-iso-surfaces, of u, v, w in (x, y)-planes and of transverse velocity-vector fields in (z, y)-planes, similar to the snapshots in figure 24.

A general view obtained from these visualizations is that, as seen in figures 22 and 23, elongated inclined structures occur and impinge on the windward face of the hill, such as the one downstream of S in figure 22. Their cross-section is roughly circular so that they cannot be the origin of the dominant w-fluctuations observed.

As demonstrated in the previous section, the streamwise velocity exhibits broad streaks at the height of the constrictions and above. In figure 24, such a streak of width about $1.5h$ impinges the windward slope of the hill at $x/h = 8$ around $z/h = 2.7$. It generates strong bi-directional spanwise motions over a relatively large distance. This is seen in figure 21(b) by the pair of positive and negative w-fluctuations labelled S. Such an event, defined by a local region of stagnation-point flow resulting from fluid impinging on a wall, is termed a 'splat' (Perot & Moin 1995). A zoom of this region is shown in figure 27, with pressure fluctuation and instantaneous velocity vectors illustrating that this is indeed a splat event. Since the impinging fluid is forced to change its direction due to the impermeability condition at the wall, tangential motion is created so that kinetic energy is transferred from the normal component

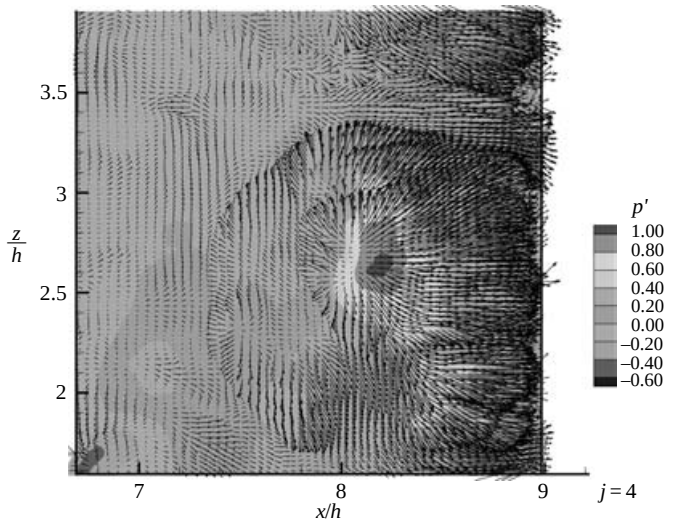

FIGURE 27. Pressure fluctuations and instantaneous velocity vectors for the same instant and grid plane as in figure 21, zoomed around the splat event observed in these plots.

to tangential ones. Due to continuity, so-called 'anti-splats' are generated close to this structure, which transport fluid back into the core of the flow. Such events are visible in figure 24 for $x/h = 8$ at $z/h = 1.0$ and 3.5. The picture in figure 24 reveals that the anti-splats can be quite narrow, as observed, for example, near $z/h = 3.5$. Animations show that this type of motion can persist for periods of the order of 0.5 times the flow-through time, which results from the large streamwise extent of the streaks in u, as observed in the horizontal cut in figure 26. The iso-pressure or iso-pressure-fluctuations, on the other hand, do not show these events, since streaks in the u-component alone, without substantial vorticity, do not create pronounced pressure minima. Splats and anti-splats were investigated in great detail by Perot & Moin (1995) who studied the interaction of turbulence with a wall in a stagnant body of fluid. In the present case, the situation is complicated by the strong mean tangential flow and the curvature of the boundary. This introduces a pronounced asymmetry between the w-fluctuations and those of u or, where the wall is inclined, those of the tangential component in streamwise direction.

To complete these observations and support them by statistical information, the spanwise auto-correlation of all velocity components has been computed at $x/h = 8$ and is shown in figure 28. Both R_{11} and R_{22} exhibit similar shapes and decay to zero within a distance of h without negative parts. It should be recalled, however, that u and v are not tangential and normal to the wall, respectively, at this location and that, hence, R_{11} and R_{22} are intimately coupled. Considering corresponding correlations at $x/h = 6$ and 8, at the same wall distance (figures 25 and 28) shows R_{11} and R_{22} at $x/h = 8$ to have a similar shape to R_{11} at $x/h = 6$. In contrast, the spanwise correlation R_{33} undergoes a substantial quantitative and qualitative change between $x/h = 6$ and 8. Thus, R_{33} develops larger values for small separation r_z/h and stronger negative values for large separation. The shape around $r_z/h = 0.5$ changes from concave at $x/h = 6$ to linear and, for $(y - y_w)/h = 0.269$, even slightly convex at $x/h = 8$. With increasing wall distance, the zero crossings of R_{33} at $x/h = 8$ move further away from the origin (from about $0.65h$ to about $0.95h$), and the negative values for large separation become more pronounced up to a distance of $(y - y_w)/h = 0.269$. This trend is

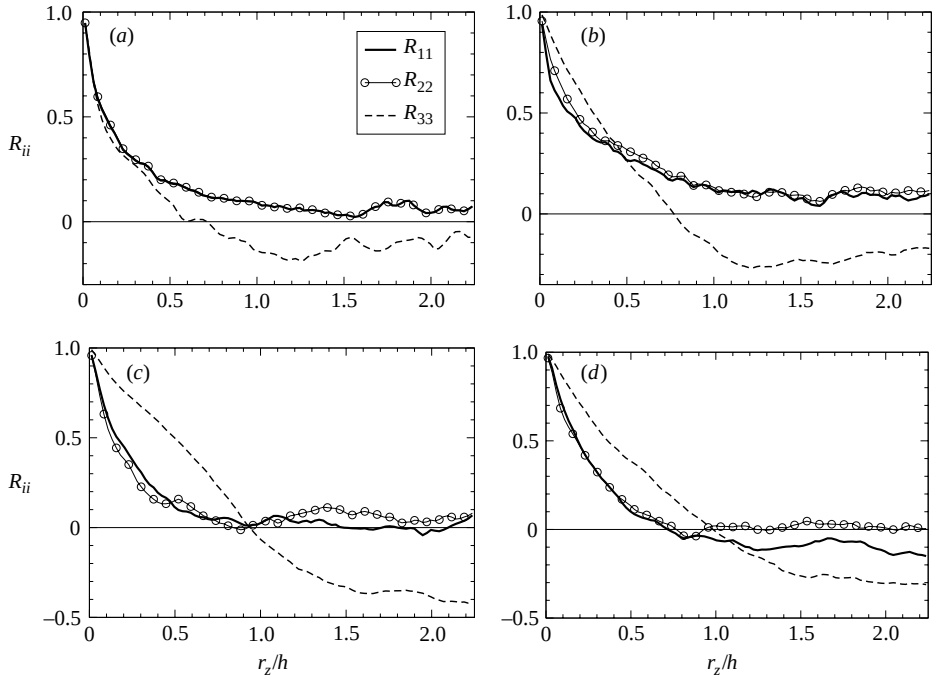

FIGURE 28. Spanwise auto-correlation functions at $x/h = 8$ determined in the same way as the data in figure 25 at four distances from the wall: (*a*) $(y - y_w)/h = 0.0027$, (*b*) $(y - y_w)/h = 0.029$, (*c*) $(y - y_w)/h = 0.269$, (*d*) $(y - y_w)/h = 0.558$, $y/h = 1.00$. The curves represent the correlations of the u-fluctuations, R_{11}, of the v-fluctuations, R_{22}, and of the w-fluctuations, R_{33}, respectively.

somewhat reversed for larger distances, as observed in the picture at $(y - y_w)/h = 0.558$. While the correlation data still exhibit some sampling error giving non-vanishing values at $r_z = L_z/2$, the data for R_{33} at $x/h = 8$ are non-negative at $r_z = L_z/2$ for physical reasons which possibly calls for a domain wider than the present one with $L_z = 4.5h$. This issue has been discussed in § 3.3.4 above which examines the influence of spanwise width.

Animations in planes $x/h = 6, 7, 7.5, 8$ show increasingly vigorous near-wall events with increasing streamwise coordinate, characterized by large spanwise motions. A snapshot is shown in figure 24(*d*). Simultaneously, the spanwise length scale of the streaks in the u-velocity component increases significantly. The resulting positive and negative spanwise motions resulting from this impingement typically exhibit a separation of about $1.5h$, which is reflected by the behaviour of R_{33} in figures 25 and 28. Since at $x/h = 8$ the wall is elevated by about half a hill height above the points at $x/h = 6$ and 7 located in the trough, this is in line with the discussion of streamwise structures in the previous section, where an increase in the size of the streaks with elevation from the bottom to a width of about this size has been observed. Associated with the large length scales in the streamwise direction is a large time scale. Thus, time-integration of the cross-sectional velocity fields at $x/h = 8$ shows large structural features to persist for periods of the order of half a flow-through time. Of course, as time progresses, the average spanwise motions decline towards zero.

Beyond $x/h = 8$, the flow accelerates further along the windward slope of the hill. Over the crest, some vortical activity in v and w is visible as shown in the plot for $x/h = 0.05$ of figure 24. The near-wall fluctuations in u are very small, however, and

confined to the close vicinity of the wall. The thickness of this layer is about 5% of the hill height only, as substantiated by figure 10, so that it can hardly be resolved in this plot.

Finally, the question is addressed as to whether the large spanwise fluctuations may be due to streamwise Görtler vortices on the concave upslope wall. In Gong *et al.* (1996) and Phillips *et al.* (1996), the possibility of the observed streamwise structures being generated by a Görtler instability is discussed, but immediately ruled out, mostly by qualitative arguments. On the other hand, Calhoun & Street (2001) conclude that this mechanism is important in the formation of streamwise vortices in their LES of flow over wavy boundaries at very low Reynolds number. They determined the distribution of the Görtler number, expressing the ratio of curvature to viscous effects, and found that the maximum of this number in front of the hill corresponded to the inception of the streamwise vortices. The Görtler number in Calhoun & Street (2001) has been computed from the present data, and the iso-lines look similar to the ones in Calhoun & Street (2001), but the maximum in front of the hill is located closer to the wall. This indicates that Görtler vortices also exist in the present flow, as seen in figure 22. However, as in Calhoun & Street (2001), these are likely to have a cross-section of circular shape and a diameter substantially smaller than h. Hence, they cannot be associated with the cross-sectional motion shown in figure 24 at $x/h = 8$ and cannot be responsible for the large spanwise fluctuations seen there. We conclude that these are mainly due to the splatting effect.

7. Conclusions

The most distinctive feature of this study is the wealth of statistical and structural information derived from two independent simulations for a flow that is, without question, physically complex, is pertinent to fluids-engineering practice and is free from uncertainties posed by inlet and outlet boundary conditions. The possibility that the restriction of the domain to a single streamwise periodic segment could have unduly constrained the turbulence structure close to the periodic boundary was effectively discounted by test computations for a domain spanning two periodic segments. Likewise, test computations with an increased distance between the spanwise boundaries indicate that any adverse effects arising from spanwise constraints are minor. This fact and the closeness of the two independent solutions obtained justify the claim that the accuracy of the results is good. Nevertheless, if costs were not an issue, a more extensive simulation domain, notably in the spanwise direction, would have been used. The cost of a simulation for a domain spanning two periodic segments and 7 hill heights in the spanwise direction, with the same resolution quality, is estimated to be about 200 000 CPU hours on a Cray T3E computer.

The fact that the present flow features separation from a curved surface, recirculation, reattachment, recovery and strong acceleration within a statistically homogeneous spanwise domain, makes the flow close to an ideal generic test case for statistical closures intended for modelling separated flow. Indeed, the results contained in this paper have already been widely exploited, both within individual validation studies and as part of broader workshop exercises directed towards modelling complex turbulent flows (Jakirlić, Jester-Zürker & Tropea 2001; Manceau & Bonnet 2003). The inclusion of budgets for all Reynolds-stress components for a fully turbulent separated flow bounded by a highly curved wall is another exceptional aspect of the present study. Not only do the budgets enhance the interpretation of the behaviour

of the stresses in relation to mean-flow and structural features, but they also provide a substantial aid to model validation and development.

While the statistical data demonstrate many familiar interactions – such as the close relationship between high strain generation and high stress in the separated shear layer – they also reveal a number of unfamiliar, indeed intriguing, features, especially close to the lower wall at which the flow separates and reattaches. Perhaps the most interesting finding is the very high level of spanwise turbulence intensity in the post-reattachment zone, especially when the flow encounters the windward side of the hill. Consistently, the budgets show that pressure–strain interaction diverts energy from both the wall-normal and streamwise components to the spanwise component, although the first two are lower than the last. In-depth analysis, based on visualizations and the examination of the flow structure, revealed these to be a result of 'splatting' of large-scale eddies originating from the shear layer above the recirculation zone. This feature is one that cannot even be resolved by second-moment closure, for the process is not compatible with isotropization-driven redistribution of turbulence energy. A further conclusion emerging from the budgets is that the separation of pressure–velocity interactions into pressure–strain and pressure–diffusion contributions is rather synthetic and can be misleading, in so far as the two components are large, both in the separated and the post-reattachment regions, have opposite signs and thus dominate the near-wall budgets of the shear stress and the wall-normal intensity. It is concluded, therefore, that this separation is not advantageous as a basis for constructing or improving turbulence models. The presentation of the stresses in terms of the second and third anisotropy invariants, forming the invariant map, shows all states to comply with Lumley's realizability constraints. In the invariant map, the near-wall flow is found to approach the two-component state along the locus associated with 'axisymmetric expansion'. This locus is normally populated by states along a free shear layer, and this is taken to imply that the near-wall layer is dominated by a structure that it inherits from the separated shear layer which feeds fluid to the near-wall region, both within the separated zone and the post-reattachment region. Only well beyond reattachment is there an indication that the near-wall layer begins to acquire properties akin to those of a log-law layer. Over most of the flow, the near-wall layer is very far from that in an attached flow.

The examination of unsteady features and instantaneous realizations show the flow to be highly disturbed in several respects. First, the position of the separation line varies greatly in time, from slightly upstream of the hill crest to about 0.5 hill heights downstream. Similarly, reattachment is highly unsteady and the flow contains large-scale unsteady structures. As noted already, one prominent structural feature identified is 'splatting' – the generation of large wall-parallel fluctuations by large-scale eddies impinging on the wall in the reattachment and post-reattachment regions. The identification of other structures, by way of a range of structure-identification methods, turned out to be a difficult undertaking, mainly because of the high Reynolds number of the flow. One interesting outcome, arising from the juxtaposition of structural features with the strain field, is that the oblique inclination of vortices in the shear layer above and downstream of the recirculation zone is linked to the orientation of the principal axes of the average deformation tensor, a relationship which does not appear to have been identified before in separated flow. In the shear layer, spanwise rollers originating from Kelvin–Helmholtz instability have been identified, and these are observed to grow to a size of order of one hill height. Also found were braid-like vortices between these rollers, which tended to be swept back by the reverse flow of the recirculation zone. Hence, the present study has contributed to the

understanding of many of the complex interactions playing a role in any turbulent separated flow.

Although it is now possible to undertake DNS studies for the flow considered herein, such studies would still be extremely costly, requiring approximately 50 million nodes and CPU resources about 50 times larger than those expended here. The benefit of doing so would be modest, however, except in so far as it would allow dissipation and other processes that are sensitive to the smallest scales to be captured explicitly. It could be argued that a much better investment of such resources would be directed towards highly resolved LES at higher Reynolds numbers and larger extent in the spanwise direction.

C. P. M. and L. T. acknowledge the financial support provided by the European Commission through the Framework V BRITE/EURAM project 'LESFOIL'. J. F. has been funded through the DFG-CNRS research initiative 'Numerical Flow Simulation'. The simulations undertaken were made possible by the provision of computer resources on the CSAR Cray T3E national facility in Manchester, through a grant from the UK Engineering and Physical Sciences Research and the availability of IBM-SP-computer resources at the Karlsruhe Computer Center. Both are gratefully acknowledged.

REFERENCES

Abe, K., Jang, Y.-J. & Leschziner, M. A. 2003 An investigation of wall–anisotropy expressions and length–scale equations for non–linear eddy–viscosity models. *Intl J. Heat Fluid Flow* **24**, 181–198.

Alam, M. & Sandham, N. D. 2000 Direct numerical simulation of short laminar separation bubbles with turbulent reattachment. *J. Fluid Mech.* **403**, 223–250.

Almeida, G. P., Durao, D. F. G. & Heitor, M. V. 1993 Wake flows behind two dimensional model hills. *Expl Thermal Fluid Sci.* **7**, 87–101.

Armenio, V. & Piomelli, U. 2000 A Lagrangian mixed subgrid–scale model in generalized coordinates. *Flow, Turbulence Combust.* **65**, 51–81.

Bell, J. H. & Mehta, R. D. 1990 Development of a two–stream mixing layer from tripped and untripped boundary layers. *AIAA J.* **28**, 2034–2042.

Breuer, M. & Rodi, W. 1994 Large eddy simulation of turbulent flow through a straight square duct and a 180° bend. In *Fluid Mechanics and its Applications* (ed. P. Voke, R. Kleiser & J. Chollet), vol. 26, pp. 273–285. Kluwer.

Buckles, J., Hanratty, T. J. & Adrian, R. J. 1984 Turbulent flow over large amplitude wavy surfaces. *J. Fluid Mech.* **140**, 27–44.

Calhoun, R. J. 1998 Numerical inverstigations of turbulent flow over complex terrain. PhD thesis, Stanford University.

Calhoun, R. J. & Street, R. L. 2001 Turbulent flow over a wavy surface: Neutral case. *J. Geophys. Res.* C **106**, 9277–9294.

Cherukat, P., Na, Y., Hanratty, T. J. & McLaughlin, J. B. 1998 Direct numerical simulation of a fully developed flow over a wavy wall. *Theoret. Comput. Fluid Dyn.* **11**, 109–134.

De Angelis, V., Lombardi, P. & Banerjee, S. 1997 Direct numerical simulation of turbulent flow over a wavy wall. *Phys. Fluids* **9**, 2429–2442.

Dejoan, A. & Leschziner, M. A. 2003 Large eddy simulation of periodically perturbed separated flow over a backward facing step. *Intl J. Heat Fluid Flow* (submitted).

Ducros, F., Nicoud, F. & Poinsot, T. 1998 Wall-adapting local eddy-viscosity models for simulations in complex geometries. In *Numerical Methods for Fluid Dynamics VI* (ed. M. J. Baines), pp. 293–299. Oxford University Computing Laboratory, Wolfson Building, Parks Road, Oxford.

Ferziger, J. H. & Peric, M. 1996 *Computational Methods for Fluid Dynamics*. Springer.

Fröhlich, J. 1990 Résolution numérique des équations de Navier–Stokes à faible nombre de Mach par méthode spectrale. PhD thesis, Université de Nice – Sophia-Antipolis.

Fröhlich, J. & Rodi, W. 2000 Introduction to Large–Eddy Simulation of turbulent flows. In *Closure Strategies for Turbulent and Transitional Flows* (ed. B. E. Launder & N. D. Sandham), chap. 8, pp. 267–298. Cambridge University Press.

Germano, M., Piomelli, U., Moin, P. & Cabot, W. H. 1991 A dynamic subgrid–scale eddy viscosity model. *Phys. Fluids* A **3**, 1760–1765.

Gong, W., Taylor, P. A. & Dörnbrack, A. 1996 Turbulent boundary-layer flow over fixed aerodynamically rough two-dimensional sinusoidal waves. *J. Fluid Mech.* **312**, 1–38.

Günther, A. & von Rohr, P. R. 2003 Large–scale structures in a developed flow over wavy terrain. *J. Fluid Mech.* **478**, 257–285.

Henn, D. S. & Sykes, R. I. 1999 Large-eddy simulation of flow over wavy surfaces. *J. Fluid Mech.* **383**, 75–112.

Hudson, J. D., Dykhno, L. & Hanratty, T. J. 1996 Turbulence production in flow over a wavy wall. *Exps. Fluids* **20**, 257–265.

Jakirlić, S., Jester-Zürker, R. & Tropea, C. (Eds.) 2001 *Proc. 9th ERCOFTAC/IAHR/COST Workshop on Refined Turbulence Modelling, October 4–5, Darmstadt, Germany*, http://www.sla.maschinenbau.tu-darmstadt.de/workshop01.html.

Jang, Y. J., Leschziner, M. A., Abe, K. & Temmermann, L. 2002 Investigation of anisotropy–resolving turbulence models by reference to highly–resolved LES data for separated flow. *Flow, Turbulence Combust.* **69**, 161.

Klostermeier, C. 2001 Correlation analysis of large structures on LES of periodic hill flow. Internal report, Institut für Hydromechanik, Universität Karlsruhe.

Lardat, R. & Leschziner, M. A. 1998 A Navier–Stokes solver for LES on parallel computers. *Tech. Rep.* University of Manchester.

Le, H. & Moin, P. 1991 An improvement of fractional step methods for the incompressible Navier–Stokes equations. *J. Comput. Phys.* **92**, 369–379.

Lilly, D. K. 1992 A proposed modification of the Germano subgrid-scale closure method. *Phys. Fluids* A **4**, 633–635.

Lumley, J. L. 1978 Computational modeling of turbulent flows. *Adv. Appl. Mech.* **18**, 123–176.

Lumley, J. L. & Newman, G. 1977 The return to isotropy of homogeneous turbulence. *J. Fluid Mech.* **82**, 161–178.

Maaß, C. & Schumann, U. 1996 Direct numerical simulation of separated turbulent flow over a wavy boundary. In *Notes on Numerical Fluid Mechanics*, vol. 52 (ed. E. H. Hirschel), pp. 227–241. Vieweg.

Manceau, R. & Bonnet, J.-P. (Eds.) 2003 *Proc. 10th ERCOFTAC/IAHR/QNET-CFD Workshop on Refined Turbulence Modelling, Laboratoire d'études Aerodynamiques, UMR CNRS 6609, Université de Poitiers, France.*

Mathey, F., Fröhlich, J. & Rodi, W. 1999 Large eddy simulation of the flow over a matrix of surface mounted cubes. In *Industrial and Environmental Applications of Direct and Large–Eddy Simulations* (ed. S. Biringen, H. Örs, A. Tezel & J. H. Ferziger). Lecture Notes in Physics, vol. 529, pp. 153–163. Springer.

Mellen, C. P. 1998 On improving the speed and the accuracy of solution of the incompressible Navier–Stokes equations. PhD thesis, University of Sidney, Australia.

Mellen, C. P., Fröhlich, J. & Rodi, W. 2000 Large eddy simulation of the flow over periodic hills. In *Proc. IMACS World Congress* (ed. M. Deville & R. Owens), *Lausanne*.

Na, Y. & Moin, P. 1998 Direct numerical simulation of a separated turbulent boundary layer. *J. Fluid Mech.* **374**, 379–405.

Nicoud, F. & Ducros, F. 1999 Subgrid-scale stress modelling based on the square of the velocity gradient tensor. *Flow, Turbulence Combust.* **62**, 183–200.

Perot, J. B. & Moin, P. 1995 Shear–free turbulent boundary layers. Part 1. Physical insights into near–wall turbulence. *J. Fluid Mech.* **295**, 199–227.

Phillips, W. R. C. & Wu, Z. 1994 On the instability of wave–catalysed longitudinal vortices in strong shear. *J. Fluid Mech.* **272**, 235–254.

Phillips, W. R. C., Wu, Z. & Lumley, J. L. 1996 On the formation of longitudinal vortices in a turbulent boundary layer over wavy terrain. *J. Fluid Mech.* **326**, 321–341.

Piomelli, U. & Chasnov, J. R. 1996 Large–eddy simulations: theory and applications. In *Turbulence and Transition Modelling* (ed. M. Hallbäck, D. S. Henningson, A. V. Johansson & P. H. Alfredson), pp. 269–331. Kluwer.

Pope, S. B. 2000 *Turbulent Flows*. Cambridge University Press.

Press, W. H., Teukolsky, S. A., Vetterling, W. T. & Flannery, B. P. 1992 *Numerical Recipes*. Cambridge University Press.

Rhie, C. M. & Chow, W. L. 1983 A numerical study of the turbulent flow past an isolated airfoil with trailing edge separation. *AIAA J.* **21**, 1225–1532.

Rodi, W., Bonnin, J. C. & Buchal, T. (Eds.) 1995 *ERCOFTAC Workshop on Data Bases and Testing of Calculation Methods for Turbulent Flows, University of Karlsruhe, Germany*.

Salvetti, M. V., Damiani, R. & Beux, F. 2001 Three-dimensional coarse large-eddy simulations of the flow above two-dimensional sinusoidal waves. *Intl J. Numer. Meth. Fluids* **35**, 617–642.

Schmitt, S., Richter, K. & Friedrich, R. 1986 Large–eddy simulation of turbulent boundary layer and channel flow at high Reynolds number. In *Direct and Large Eddy Simulation, Proc. Euromech Coll. 199, München, FRG, 30 Sept.–2 Oct. 1985* (ed. U. Schumann & R. Friedrich). Notes on Numerical Fluid Mechanics, vol. 15, pp. 161–176. Vieweg.

Silveira-Neto, A., Grand, D., Métais, O. & Lesieur, M. 1993 A numerical investigation of the coherent structures of turbulence behind a backward–facing step. *J. Fluid Mech.* **256**, 1–25.

Steger, J. L. & Sorenson, R. L. 1979 Automatic mesh point clustering near a boundary in grid generation with elliptic partial differential equations. *J. Comput. Phys.* **33**, 405–410.

Stone, H. L. 1968 Iterative solution of implicit approximations of multidimensional partial differential equations for finite difference methods. *SIAM J. Numer. Anal.* **5**, 530–558.

Temmerman, L. 2004 Large eddy simulation of separating flow from curved surfaces. PhD thesis, Department of Engineering, Queen Mary and Westfield University of London, University of London.

Temmerman, L., Leschziner, M. A., Ashworth, M. & Emerson, D. 2000 LES applications on parallel systems. In *Parallel Computational Fluid Dynamics 2000* (ed. A. Ecer, J. Periaux & N. Satofuka). Elsevier.

Temmerman, L., Leschziner, M. A., Mellen, C. P. & Fröhlich, J. 2003 Investigation of wall–function approximations and subgrid–scale models in Large Eddy Simulation of separated flow in a channel with streamwise periodic constrictions. *Intl J. Heat Fluid Flow* **24**, 157–180.

Wang, C., Yang, Y. A. & Leschziner, M. J. 2004 Modelling two- and three-dimensional separation from curved surfaces with anisotropy-resolving turbulence closures. *Intl J. Heat Fluid Flow* **25**, 499–512.

Werner, H. & Wengle, H. 1993 Large–Eddy Simulation of turbulent flow over and around a cube in a plane channel. In *Selected Papers from the 8th Symposium on Turbulent Shear Flows* (ed. F. Durst, R. Friedrich, B. Launder, F. Schmidt, U. Schumann & J. Whitelaw), pp. 155–168. Springer.

Wu, X. & Durbin, P. A. 2001 Evidence of longitudinal vortices evolved from distorted wakes in a turbine passage. *J. Fluid Mech.* **446**, 199–228.

Zdravkovich, M. M. 1997 *Flow Around Circular Cylinders*. Oxford University Press.

Zedler, E. A. & Street, R. L. 2001 Large-eddy simulation of sediment transport: currents over ripples. *J. Hydr. Engng* **127**, 444–452.